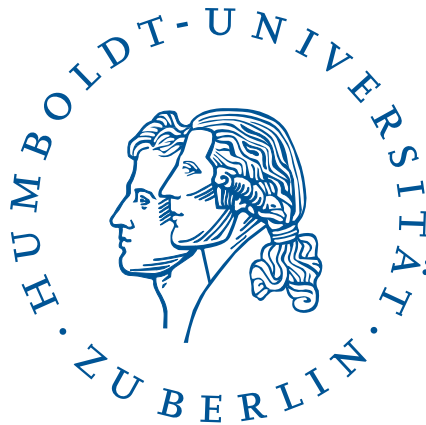# All-Electron Many-Body Approach to X-Ray Absorption Spectroscopy

MASTERARBEIT

zur Erlangung des akademischen Grades
Master of Science
(M. Sc.)
im Fach Physik

eingereicht an der
Mathematisch-Naturwissenschaftlichen Fakultät I
Institut für Physik
Humboldt-Universität zu Berlin

von
Herrn Christian Vorwerk
geboren am 25.09.1989 in Werl

Gutachter:

1. *Prof. Dr. Claudia Draxl*
2. *Prof. Dr. Kurt Busch*

eingereicht am: *13. April 2016*

Acknowledgement

First and foremost, I want to thank Claudia Draxl for her guidance and support during my Master project. Furthermore, I want to thank her for the oppurtinities she provided for me in the last years.

I am indebted to Caterina Cocchi, who was always available for discussion and feedback. This project would not have been possible without her.

Many thanks go to Dmitrii Nabok and Andris Gulans for their help with my implementation, Olga Turkina for her support on the study of TiO_2, and all the members of Claudia Draxl's research group.

Contents

List of Figures

Part I

Theoretical Background

1. Introduction

Light-matter interactions are key processes to understand the fundamental properties of matter. The search for new materials in photovoltaics and optoelectronics has gone hand in hand with the tremendous progress of experimental techniques in the last decade. Simultaneously, theoretical methodologies have been greatly advanced which allow for accurately simulating light absorption from first principles, i.e. without the aid of adjustable parameters. The development of approaches beyond the single-particle approximation have resulted in accurate descriptions of the interaction of matter with optical radiation for a wide range of materials and experimental techniques. Such methods, for example based on time-dependent density functional theory [14] or many-body perturbation theory [53], are now regularly employed to describe optical spectra of extended periodic systems and aperiodic systems alike.

Core-level excitations on the other hand are still primarily described in the independent-particle picture. The so-called *core-hole approximation* [43] (sometimes also called *final state rule* approximation) is most commonly used to calculate x-ray absorption spectra. In this approach, an electron is removed from the core state and placed in the conduction band. Then, the electronic structure of the system is calculated by a ground-state method, such as density functional theory, and the absorption spectra are obtained as the projected unoccupied density of states of the absorbing atom. In order to reduce unphysical interactions between different core holes, large unit cells are used in these calculations. Within this approach, fairly accurate results have been obtained for K egde spectra. A more crude approach is the *Z+1* approximation[1][16][26], in which a proton is added to the absorbing atom to simulate the Coulomb potential of the core-hole. Calculations have also been performed with partial core holes [42]. The core-hole approach has been implemented in several density functional packages [9][22]. However, despite the good results of the core-hole approximation for K edge absorption spectra [48][29][30], severe limitations appear when going to transitions from states with non-zero angular momentum [20]. The most notable example is the $L_{2,3}$-egde absorption spectrum of the $3d$ transition metals [82][77][39], where the branching ratio between the L_2 and L_3 spectra within the independent-particle approximation are in strong disagreement with experimental results. It was also shown that core-hole calculations are insufficient in describing accurately core-level spectra of shallow core states [50], even at the K edge. In these cases, the core-hole spectra underestimate binding energies in comparison with experiment. Examples are the Li K edge in the lithium halides and Al $L_{2,3}$ edge spectra of AlP, AlAs and AlN [51].

The description is significantly improved, once many-body effects are explicitly included. For finite systems, many-body wavefunction-based methods have been employed to x-ray absorption spectroscopy, such as the all-electron configuration interaction method [28][47] and the exact-diagonalization method [15]. These methods have the drawback that they can only treat small clusters and can not be extended to periodic systems. For extended systems, the many-body perturbation theory is a more effective approach. Here, core hole and excited electron are described as interacting quasiparticles dressed with the full interactions of the many-body system. The absorption spectrum can then be obtained by solving the *Bethe-Salpeter equation*, the equation of motion for the two-particle Green's function. Thus, it reproduces the dynamic electron-hole interaction missing in

---

[1]The approximation is called the *optical alchemy approximation* in Ref. [26], a name worth repeating.

the independent-particle picture. It has been shown [3] [62], that the screening of the core hole, as well as the inclusion of exchange interactions, induces the differences between core-hole and BSE calculations. Since such an approach couples localized core states and extended conduction states, few implementation of this approach to core excitations exist [68][76][39][52].

As such, there are currently two approaches to core excitations in solids: While most implementations, which excplicitely obtain core states from the crystal potential, use the core-hole approximation to include excitonic effects, most implementations, which treat many-body effects within the BSE approach, obtain core states from an atomistic approximation. Implementing the BSE approach within the all-electron code **exciting** [23] bridges the gap between these approaches. Combining excplicit descriptions of the core electrons with a careful treatment of the electron-hole interaction, this approach is applicable to absorption edges irregardless of the angular momentum and spin-orbit coupling of the core states. Implemented in a state-of-the-art density functional package, it makes use of the highly accurate band structure results obtained in full-potential (L)APW+LO calculations. Combinations with band structure methods beyond density functional theory, such as many-body corrections through G_0W_0, are possible. Lastly, the implementation in a well-documented open-source code package makes this approach available to the community, hopefully stimulating a wide application of this approach to solid materials.

The work is organized as follows: The first part is focused on the theoretical background and the implementation of the Bethe-Salpeter equation (BSE) approach to x-ray absorption spectroscopy. In Chapter 2, density functional theory (DFT) is reviewed, focusing on the basic theorems and the expansion of the resulting equations in a basis set. The many-body perturbation theory (MBPT) will be discussed in Chapter 3. The Derivation of this method within this chapter are limited to the parts that are most relevant in this work. Chapter 4 presents the application of the MBPT approach to core excitations. Treatment of core and conduction electrons in the code will be introduced and the effective Hamiltonian for the electron-hole system si discussed in detail. Derivations for the reformulation of matrix elements between Bloch states and the atomic separation of the BSE Hamiltonian are provided. The implementation of the BSE Hamiltonian is described in Chapter 5. The main focus of this chapter will be on the planewave matrix elements. To demonstrate the capabilities of this methodology, it is applied to the Ti $L_{2,3}$ edge absorption spectrum of rutile TiO_2 in Chapter 6.
The second part of the thesis is devoted to the x-ray absorption spectroscopy of hybrid organic-inorganic perovskite $CH_3NH_3PbI_3$: In Chapter 7, the material is introduced, showing its practical relevance and theoretical challenges. Chapter 8 provides a discussion of its electronic structure in comparison to the binary compound PbI_2. I $L_{2,3}$ edge spectra are discussed in Chapter 9, Pb $M_{4,5}$ spectra in Chapter 10. In the discussions of the core-level spectra, a comparison is drawn between results obtained from solutions of the BSE and those obtained in the independent-particle (IP) approximation.

2. Density Functional Theory

All properties of solid state materials can, in principle, be obtained from the Schrödinger equation of the electrons and nuclei, that the system is composed of. Unfortunately, electrons and nuclei form a strongly interacting many-body system with an immense amount of degrees of freedom, making a solution of the full equation virtually impossible. A first simplification is introduced by the Born-Oppenheimer approximation, which allows for the decoupling of the electronic and nuclear degrees of freedom. Thereby, the problem of determining the full wavefunction of the system is reduced to the problem of determining the electronic wavefunction for a given set of nuclear positions. The equation to be solved is now[1]

$$\left[-\sum_i \frac{\nabla_i^2}{2} - \sum_{i,I} \frac{Z_I}{|\mathbf{r}_i - \mathbf{R}_I|} + \frac{1}{2}\sum_{i \neq j} \frac{1}{|\mathbf{r}_i - \mathbf{r}_j|} \right] \Psi(\mathbf{r}_1, \mathbf{r}_2, ..., \mathbf{r}_N) = E\Psi(\mathbf{r}_1, \mathbf{r}_2, ..., \mathbf{r}_N),$$

(2.1)

which governs the behaviour of the electronic wavefunction $\Psi(\mathbf{r}_1, .., \mathbf{r}_N)$ for a system of N interacting electrons in the potential of nuclei with atomic number Z_I at position $\mathbf{R}_I$.

One approach to obtain the electronic wavefunction is to expand it in terms of single-electron wavefunctions, which leads to a system of N coupled differential equations. This approach, called the configuration interaction method, is computationally very costly and usually only applied to smaller systems.

A different approach is offered by the Density Functional Theory (DFT): Instead of the electronic wavefunction $\Psi(\mathbf{r}_1, .., \mathbf{r}_N)$, the density $n(\mathbf{r})$ is used as the basic quantity. All observables are then expressed not as expectation values of the electronic wavefunction, but as functionals of the density. This tremendously reduces the complexity of the problem as the density depends only on three variables, whereas the wavefunction depends on $3N$ coordinates of the electrons [2]. The validity of this formalism for the ground state is guaranteed by the Hohenberg-Kohn theorem.

2.1 Hohenberg-Kohn Theorem

The basic lemma to the Hohenberg-Kohn theorem [27] states that the external potential $v_{ext}(\mathbf{r})$ is a unique functional of the electron density $n(\mathbf{r})$ of an inhomogeneous electron gas. By virtue of this, the total energy of this system can be expressed as

$$E[n(\mathbf{r})] = \int v_{ext}(\mathbf{r})n(\mathbf{r})d^3r + F[n(\mathbf{r})],$$

(2.2)

where $F[n(\mathbf{r})]$ is a potential-independent functional that takes into account the kinetic energy and the interaction of the electron. The ground-state energy E_0 of the Schrödinger equation $\hat{H}\Psi = E\Psi$ can be determined by the Rayleigh-Ritz variational principle:

$$E_0 = \min_{\tilde{\Psi}} \frac{\langle \tilde{\Psi}|\hat{H}|\tilde{\Psi}\rangle}{\langle \tilde{\Psi}|\tilde{\Psi}\rangle},$$

(2.3)

---

[1]Throughout this thesis, atomic units are used: $\hbar = 1$, $e = 1$, $m_e = 1$, $a_0 = 1$

[2]The spin of the electrons is ignored in this introduction. DFT can be extended straightforwardly to spin-polarized systems.

where $\tilde{\Psi}$ is a trial wavefunction. The Hohenberg-Kohn theorem states that this minimization with respect to a trial wavefunction can be replaced by a minimization with respect to a trial density $\tilde{n}(\mathbf{r})$:

$$E_0 = \min_{\tilde{n}(\mathbf{r})} E[\tilde{n}(\mathbf{r})] = \min_{\tilde{n}(\mathbf{r})} \left[\int v_{ext}(\mathbf{r})\tilde{n}(\mathbf{r})d^3r + F[\tilde{n}(\mathbf{r})] \right]. \tag{2.4}$$

2.2 Kohn-Sham Equations

While the Hohenberg-Kohn theorem ensures that the ground state energy can be determined by a minimization with respect to trial densities, it does not provide the form of the functional $F[n(\mathbf{r})]$ in Eq. (2.2). Kohn and Sham [33] proposed a separation into three contributions:

$$F[n(\mathbf{r})] = T_s[n(\mathbf{r})] + \frac{1}{2} \int \int \frac{n(\mathbf{r})n(\mathbf{r}')}{|\mathbf{r} - \mathbf{r}'|} d^3r d^3r' + E_{xc}[n(\mathbf{r})], \tag{2.5}$$

where the first term is the kinetic energy of non-interacting electrons, the second term the Hartree energy and the third term the exchange-correlation functional. This functional includes the interactions of the electrons beyond the Hartree energy and the kinetic energy difference between the non-interacting and the interacting electrons. The functional derivative of Eq. (2.2), under the condition of constant particle number N, yields a set of equations resembling the Schrödinger equation of non-interacting electrons in an effective potential. Using a Lagrange multiplier ϵ, one obtains:

$$\delta E[n(\mathbf{r})] = \int \left(\frac{\delta T[n(\mathbf{r})]}{\delta n(\mathbf{r})} + \int \frac{n(\mathbf{r}')}{|\mathbf{r} - \mathbf{r}'|} d^3r' + \frac{\delta E_{xc}[n(\mathbf{r})]}{\delta n(\mathbf{r})} + v_{ext}(\mathbf{r}) - \epsilon \right) \delta n(\mathbf{r}) d^3r. \tag{2.6}$$

With this equation, the problem of N interacting electrons in an external potential can be mapped to that of N non-interacting electrons in an effective potential $v_{eff}(\mathbf{r})$:

$$v_{eff}(\mathbf{r}) = v(\mathbf{r}) + \int \frac{n(\mathbf{r}')}{|\mathbf{r} - \mathbf{r}'|} d^3r' + \frac{\delta E_{xc}[n(\mathbf{r})]}{\delta n(\mathbf{r})}. \tag{2.7}$$

The first term in the sum is the external Coulomb potential of the nuclei, the second is the Hartree-potential, which describes the mean-field interaction of the electrons, and the third term takes into account the many-body effects beyond the Hartree-potential, and is called exchange-correlation potential. One can now obtain the ground-state density and energy by solving a set of non-interacting Schrödinger equations:

$$\left[-\frac{1}{2}\nabla^2 + v_{eff}(\mathbf{r}) \right] \psi_i = \epsilon_i \psi_i(\mathbf{r}). \tag{2.8}$$

It is important to note, that these so called Kohn-Sham eigenstates $\psi_i(\mathbf{r})$ only yield the correct groundstate density and energy. The Kohn-Sham energy eigenvalues and wavefunctions can not be seen as the single-particle energies and wavefunctions of the many-body system. The density is obtained as:

$$n(\mathbf{r}) = \sum_{i=1}^{N} |\psi_i(\mathbf{r})|, \tag{2.9}$$

and the ground state energy $E_0[n]$ as:

$$E_0[n] = -\sum_{i=1}^{N} \int \psi_i(\mathbf{r}) \frac{\nabla^2}{2} \psi_i(\mathbf{r}) d^3r + \frac{1}{2} \int \frac{n(\mathbf{r})n(\mathbf{r}')}{|\mathbf{r}-\mathbf{r}'|} d^3r d^3r' + \int v_{ext}(\mathbf{r})n(\mathbf{r})d^3r + E_{xc}[n].$$
(2.10)

The expression for the functional $E_{xc}[n(\mathbf{r})]$ is unknown, but many approximations have been developed. In the following, the two most prominent groups of approximations will shortly be summarized: In the Local Density Approximation (LDA) [55], the functional is expressed as

$$E_{xc}^{LDA}[n(\mathbf{r})] = \int e_{xc}(n(\mathbf{r}))n(\mathbf{r})d^3r,$$
(2.11)

where $e_{xc}(n(\mathbf{r}))$ is the exchange-correlation energy per particle of the homogeneous electron gas. In order to take into account some of the non-locality of the functional, in the generalized gradient approximation (GGA) [56][57] the exchange-correlation functional is written as:

$$E_{xc}^{GGA}[n(\mathbf{r})] = \int f(n(\mathbf{r}), |\nabla n(\mathbf{r})|)n(\mathbf{r})d^3r,$$
(2.12)

where f is a function of the density $n(\mathbf{r})$, as well as the gradient ∇n. Several of these functions f have been developed, one popular example is the so-called PBE functional [56], which is derived by using properties of the exact exchange-correlation potential.

2.3   Basis-set Expansion

For periodic materials with a set of lattice vectors $\{\mathbf{R}_i\}$, the Kohn-Sham wavefunctions at a wavevector $\mathbf{k}$ obey the Bloch conditions:

$$\psi_{\mathbf{k}}(\mathbf{r} + \mathbf{R}_i) = e^{i\mathbf{k}\mathbf{R}_i}\psi_{\mathbf{k}}(\mathbf{r}).$$
(2.13)

In order to transforms the differential Kohn-Sham equation (2.8) into a set of algebraic equations, the Kohn-Sham wavefunctions are expanded in a basis set $\phi_{i\mathbf{k}}$:

$$\psi_{\mathbf{k}}(\mathbf{r}) = \sum_i c_{i\mathbf{k}}\phi_{i\mathbf{k}}(\mathbf{r}).$$
(2.14)

This yields a matrix equation

$$[H(\mathbf{k}) - \epsilon_i S(\mathbf{k})]\,\tilde{c}(\mathbf{k}) = 0,$$
(2.15)

which has to be solved for every $\mathbf{k}$-point within the first Brillouin zone. The Hamiltonian matrix $H(\mathbf{k})$ is introduced with the matrix elements

$$H^{ij}(\mathbf{k}) = \int_\Omega (\phi_{i\mathbf{k}}(\mathbf{r}))^* \left[-\frac{1}{2}\nabla^2 + v_{eff}(\mathbf{r})\right] \phi_{j\mathbf{k}}(\mathbf{r})d^3r,$$
(2.16)

and the overlap matrix $S(\mathbf{k})$ with the elements

$$S^{ij}(\mathbf{k}) = \int_\Omega (\phi_{i\mathbf{k}}(r))^* \phi_{j\mathbf{k}}(\mathbf{r})d^3r.$$
(2.17)

Here, Ω denotes the unit cell volume. The Hamiltonian and overlap matrices have the size $M \times M$, where M is the number of basis functions. The vector $\tilde{c}(\mathbf{k})$ has the length M for a given k-point. The Kohn-Sham eigenvalues are now obtained by diagonalizing the matrix Eq. (2.15). For a complete basis set, the expression of Eq. (2.14) is exact. In practice, the number of basis functions is limited, and the accuracy of the results therefore depends on the choice of basis functions.

The (L)APW+LO basis set [70] is developed to give an accurate description of the wavefunction both in the regions of the unit cell, where the wavefunction is varying slowly (and is therefore well described by planewaves), and in regions close to the atomic positions, where the wavefunction varies rapidly. Therefore in this basis, the unit cell is divided in two regions: The atomic spheres (MT) are non-overlaping spheres of radius $\mathbf{R}_\alpha$ centered on the atom labeled α, the interstitial space (I) is the space between these spheres (see Fig. (9.2)). The Kohn-Sham wavefunctions $\psi_{i\mathbf{k}}$ are then expanded in basis functions $\phi_{\mathbf{G}+\mathbf{k}}$, where $\mathbf{G}$ are the reciprocal lattice vectors. The basis set is given by planewaves in the interstitial region, which are augmented with

Figure 2.1: Partition of the unit cell in the LAPW method.

atomic-like functions within the sphere. In the augmented planewave (APW) method, the basis functions are expressed as

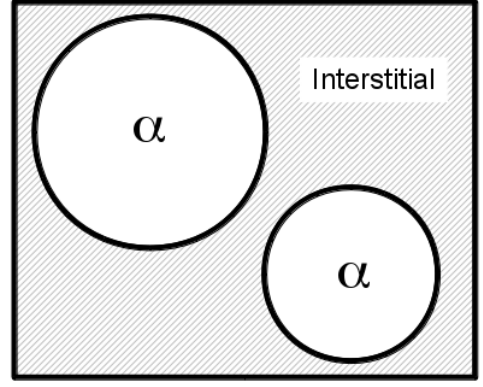$$\phi_{\mathbf{G}+\mathbf{k}}(\mathbf{r}) = \begin{cases} \sum_{lm} A_{lm\alpha}^{\mathbf{G}+\mathbf{k}} u_{l\alpha}(r_\alpha; \epsilon) Y_{lm}(\hat{\mathbf{r}}_\alpha) & \text{for } r_\alpha \leq R_{MT} \\ \dfrac{1}{\sqrt{\Omega}} e^{i(\mathbf{G}+\mathbf{k})\mathbf{r}} & \text{for } \mathbf{r} \in I \end{cases} . \qquad (2.18)$$

Imposing continuity conditions at the sphere boundaries yields the coefficients $A_{lm\alpha}^{\mathbf{G}+\mathbf{k}}$. One notices that the basis functions within the muffin-tin spheres depend on the energy ϵ of the state. The radial functions are obtained from the radial Schrödinger equation in the spherically averaged Kohn-Sham potential $v_0(r)$:

$$\left[-\frac{1}{2}\frac{d}{dr^2} + \frac{l(l+1)}{2r^2} + v_0(r) - \epsilon_{l\alpha} \right] (ru_{l\alpha}) = 0. \qquad (2.19)$$

Thus the diagonalization of the Kohn-Sham Hamiltonian is a non-linear eigenvalue problem. In order to linearize the eigenvalue problem, the radial functions can be evaluated at fixed *reference energies* $\epsilon_{l\alpha}$. A straightforward way to reduce the error introduced by this linearization, is the expansion of the radial functions to first order in the energies as $u_{l\alpha}(r_\alpha; \epsilon) \approx u_{l\alpha}(r_\alpha; \epsilon_{l\alpha}) + (\epsilon_{l\alpha} - \epsilon)\dot{u}_{l\alpha}(r; \epsilon_{l\alpha})$, where $\dot{u}_{l\alpha}$ denotes the derivative of the radial functions with respect to the energy. In this spirit, the radial functions in the linearized augmented planewave (LAPW) [2] basis in the MT sphere are obtained as

$$\phi_{\mathbf{G}+\mathbf{k}}(\mathbf{r}) = \sum_{lm} \left[A_{lm\alpha}^{\mathbf{G}+\mathbf{k}} u_{l\alpha}(r_\alpha; \epsilon_{l\alpha}) + B_{lm\alpha}^{\mathbf{G}+\mathbf{k}} \dot{u}_{l\alpha}(r_\alpha; \epsilon_{l\alpha}) \right] Y_{lm}(\hat{\mathbf{r}}_\alpha). \qquad (2.20)$$

Here, the coefficients $A_{lm\alpha}^{\mathbf{G}+\mathbf{k}}$ and $B_{lm\alpha}^{\mathbf{G}+\mathbf{k}}$ are obtained by the condition that the basis function is continous in value and slope at the sphere boundaries.

A different approach to the linearization is chosen in the APW+LO approach [71]: The basis functions are evaluated at fixed reference energies as

$$\phi_{\mathbf{G}+\mathbf{k}}(\mathbf{r}) = \sum_{lm} A_{lm\alpha}^{\mathbf{G}+\mathbf{k}} u_{l\alpha}(r_\alpha; \epsilon_{l\alpha}) Y_{lm}(\hat{\mathbf{r}}_\alpha), \qquad (2.21)$$

and the linearization error is reduced by introducing new basis functions, which are confined within the muffin-tin spheres. These additional basis functions, called local orbitals

(LO) [69], ϕ_μ have the form:

$$\phi_\mu(\mathbf{r}) = \begin{cases} \delta_{\alpha\alpha_\mu}\delta_{ll_\mu}\delta_{mm_\mu} \left[a_\mu u_{l\alpha}(r_\alpha; \epsilon_{l\alpha}) + b_\mu \dot{u}_{l\alpha}(r_\alpha; \epsilon_{l\alpha})\right] Y_{lm}(\hat{\mathbf{r}}_\alpha) & \text{for } r_\alpha \leq R_{MT} \\ 0 & \text{for } \mathbf{r} \in I \end{cases},$$

(2.22)

where a_μ and b_μ are defined by the normalization to one and the condition that the function vanishes at the sphere boundary.

3. Many-Body Perturbation Theory

Absorption spectroscopy probes neutral electronic excitations of a system: The absorption of a photon excites an electron to the unoccupied states of the system, leaving behind a 'hole', i.e. a state previously occupied by the electron. The determination of the absorption spectrum requires that two different process are taken into account: (i) Due to the interaction of the excited electron and the hole with the other electrons in the many-body system, a description in single-particle states is in general not possible. To retain the single-particle picture, *quasiparticles* are introduced. These quasiparticles are effective states dressed by the full interaction of the many-body system. They behave like weakly interacting particles in an effecive potential. (ii) The quasielectron and quasihole are not independent particles, but interact through the Coulomb potential, which is screened by the remaining electrons of the system. Thus, a two-particle Hamiltonian, which can treat quasielectron and quasihole simultaneously, is needed.

An approach, which describes the interaction of two quasiparticles, is the many-body perturbation theory (MBPT). Using a two-particle Green's function formalism, an effective two-particle Hamiltonian is derived. The interaction with the many-body system is included through the screened Coulomb potential. Thus, this approach maps the correlated many-body problem on a set of single-particle problems. For a more detailed treatment of MBPT and its application to optical spectroscopy, see [58], [65],[64], and [53]. The following chapter provides the basic concepts and properties of this approach, as necessary in the scope of this thesis.

3.1 Dielectric Response

In the linear response to an electromagnetic field, the components $D_i(\mathbf{r}, \omega)$ of the electric displacement are related to the components of the electric field $E_j(\mathbf{r}, \omega)$ by the dielectric tensor $\epsilon_{ij}(\mathbf{r}, \mathbf{r}', \omega)$:

$$D_i(\mathbf{r}, \omega) = \int d^3 r' \epsilon_{ij}(\mathbf{r}, \mathbf{r}', \omega) E_j(\mathbf{r}, \omega). \tag{3.1}$$

The dielectric tensor contains the full information of the response of a specific system to an external electromagnetic field in linear order. It is often reformulated in terms of the complete polarization $P(\mathbf{r}, \mathbf{r}', \omega)$:

$$\epsilon^{-1}(\mathbf{r}, \mathbf{r}', \omega) = \delta(\mathbf{r}, \mathbf{r}') + \int d^3 r'' v(\mathbf{r}, \mathbf{r}'') P(\mathbf{r}', \mathbf{r}'', \omega), \tag{3.2}$$

where $v(\mathbf{r}, \mathbf{r}')$ is the bare Coulomb potential. The complete polarization describes the change of the charge density with respect to the external potential. In materials with translational symmetries, the dielectric tensor can be Fourier-transformed into reciprocal space:

$$\epsilon(\mathbf{r}, \mathbf{r}', \omega) = \frac{1}{\Omega} \sum_q \sum_{\mathbf{G}\mathbf{G}'} e^{-i(\mathbf{q}+\mathbf{G})\mathbf{r}} \epsilon(\mathbf{q}+\mathbf{G}, \mathbf{q}+\mathbf{G}', \omega) e^{i(\mathbf{q}+\mathbf{G}')\mathbf{r}'}, \tag{3.3}$$

where $\mathbf{q}$ is a vector from the first Brillouin zone, $\mathbf{G}$ and $\mathbf{G}'$ are reciprocal lattice vectors and Ω is the volume of the crystal. In optical spectroscopy, one is interested in the average response of the system to the incoming light, not the variation of the response on an atomic scale. The *macroscopic dielectric tensor* is therefore define as $\epsilon_M(\mathbf{q}, \omega)$, which is

obtained from the $\mathbf{G} = \mathbf{G}' = 0$ component of the inverse microscopic tensor, denoted as $\epsilon^{-1}(\mathbf{q}, \mathbf{q}, \omega)$:

$$\epsilon_M(\mathbf{q}, \omega) = \frac{1}{\epsilon^{-1}(\mathbf{q}, \mathbf{q}, \omega)}. \tag{3.4}$$

The determination of the macroscopic dielectric tensor requires the calculation of the complete polarization $P(\mathbf{r}, \mathbf{r}', \omega)$, which in turn yields the inverse microscopic dielectric function $\epsilon^{-1}(\mathbf{r}, \mathbf{r}', \omega)$, following Eq. (3.3). Matrix inversion then yields the macroscopic dielectric function in Eq. (3.4).

3.2 Bethe-Salpeter Equation

In the Bethe-Salpeter equation (BSE) approach, the calculation of the polarization is replaced by the determination of the two-particle correlation function. This allows one to use a Green's-function based approach, which includes the electron-hole interaction and hence reproduces excitonic effects. Using the notation $(1) = (\mathbf{r}_1, t_1)$, the complete polarization is connected to the two-particle correlation function $L(1, 2, 3, 4)$ by [58]

$$P(1, 2) = -iL(1, 1, 2, 2). \tag{3.5}$$

The two-particle correlation function is defined as

$$L(1, 1', 2, 2') = G_2(1, 1', 2, 2') - G(1', 2')G(1, 2), \tag{3.6}$$

and is thus the two-particle Green's function $G_2(1, 1', 2, 2')$, which excludes the disconnected part represented by the product of single-particle Green's functions $G(1', 2')G(1, 2)$. The Bethe-Salpeter equation is a Dyson's-like equation for the two-particle correlation function:

$$L(1, 1', 2, 2') = L_0(1, 1', 2, 2') + \int d(3, 3', 4, 4') L_0(1, 1', 3, 3') \Xi(3, 3', 4, 4') L(4, 4', 2, 2'). \tag{3.7}$$

Tthe function L_0 is introduced, describing the independent motion of two-particles

$$L_0(1, 1', 2, 2') = G(1', 2')G(1, 2), \tag{3.8}$$

and the kernel Ξ as the functional derivative of the Hartee energy V_H and the self energy Σ with respect to the single-particle Green's function:

$$\Xi(3, 3', 4, 4') = \frac{\delta[V_H(4, 4') + \Sigma(4, 4')]}{\delta G(3, 3')} \tag{3.9}$$

In order to calculate the interaction kernel Ξ, approximations to the self energy Σ are required. A common assumption is to insert the self energy of the G_0W_0-approach into Eq. (3.9).[1] A full derivation of the self energy and the G_0W_0 approximation does not lie within the scope of this thesis, more detailed treatments can be found in [18], [25], [65] and [58]. In the following, the central equations of the G_0W_0 approach are stated, as they are needed in the screened interaction approximation. The self energy in this approximation is given as

$$\Sigma(1, 2) = iG(1, 2)W(1, 2), \tag{3.10}$$

---

[1]This approach is known as the *screened interaction approximation* to the interaction kernel Ξ.

where $W(1, 2)$ is the dynamically screened Coulomb interaction obtained by

$$W(1, 2) = \int \epsilon^{-1}(1, 3)v(1, 3)d(3), \tag{3.11}$$

using the dielectric function $\epsilon(1, 2)$ in the RPA approximation:

$$\epsilon(1, 2) = \delta(1, 2) + i \int v(1, 3)G(2, 3)G(3, 2)d(3). \tag{3.12}$$

The Hartree energy $V_H(4, 4')$ is also expressed in terms of the one-particle Green's function:

$$V_H(4, 4) = -i\delta(4, 4') \int G(5, 5^+)v(5, 4)d(5). \tag{3.13}$$

If the self energy of Eq.(3.10) and the Hartee energy of Eq.(3.13) are inserted into Eq. 3.9, one obtains

$$\Xi(3, 3', 4, 4') = -i\delta(3, 3')\delta(4, 4')v(3, 4) + i\delta(3, 4)\delta(3', 4')W(3, 3') + iG(1, 2)\frac{\delta W(1, 2)}{\delta G(4, 3)}. \tag{3.14}$$

In what is called the *ladder approximation* to the Bethe-Salpeter equation, the last term of this approximation is neglected, since this term is small compared to the first two contributions [67]. In this approximation, one therefore use

$$\Xi(3, 3', 4, 4') = -i\delta(3, 3')\delta(4, 4')v(3, 4) + i\delta(3, 4)\delta(3', 4')W(3, 3'). \tag{3.15}$$

3.3   BSE as an Eigenvalue Problem

In the following, a reformulation of the Bethe-Salpeter equation (3.7) from an integral equation to a matrix eigenvalue problem will be presented, which will allow for the numerical determination of $L(1, 1', 2, 2')$. The interested reader is directed to Refs. [58] and [65] for a more detailed treatment.

The two-particle correlation function of a crystal has to obey translational symmetry, i.e. for a given lattice vector $\mathbf{R}$, the equation

$$L(\mathbf{r}_1 + \mathbf{R}, \mathbf{r}_1' + \mathbf{R}, \mathbf{r}_2 + \mathbf{R}, \mathbf{r}_2' + \mathbf{R}) = L(\mathbf{r}_1, \mathbf{r}_1', \mathbf{r}_2, \mathbf{r}_2') \tag{3.16}$$

has to be fulfilled. Therefore, one can reformulate the function as a sum of $L_\mathbf{q}(1, 1', 2, 2')$, where $\mathbf{q}$ is a vector from the first Brillouin zone and each function $L_\mathbf{q}$ has the full symmetry of the lattice:

$$L(1, 1', 2, 2') = \sum_\mathbf{q} L_\mathbf{q}(1, 1', 2, 2'). \tag{3.17}$$

Since the interest of this thesis lies in the respone in the optical limit, $\mathbf{q} \to 0$, in the following only the L_0 contribution is considered and it is denoted $L(1, 1', 2, 2')$. As this function has translational symmetry, it can be expanded in the basis of the quasiparticle wavefunctions. These wavefunctions are approximated by the Kohn-Sham wavefunctions and write

$$L(\mathbf{r}_1, \mathbf{r}_1', \mathbf{r}_2, \mathbf{r}_2') = \sum_{i_1, i_2, i_3, i_4} \psi_{i_1}^*(\mathbf{r}_1)\psi_{i_2}(\mathbf{r}_1')\psi_{i_3}(\mathbf{r}_2)\psi_{i_4}^*(\mathbf{r}_2')L_{(i_1 i_2)(i_3 i_4)}. \tag{3.18}$$

This yields a matrix equation for the correlation function:

$$L_{(i_1 i_2)(i_3 i_4)}(\omega) = \sum_{j_3 j_4} \left[1 - L^0(\omega)\Xi \right]^{-1}_{(i_1 i_2)(j_3 j_4)} L^0_{(j_3 j_4)(i_3 i_4)}. \tag{3.19}$$

The independent-particle correlation function $L^0(1, 1', 2, 2')$ can now be rewritten in this basis. Using also the Green's function in the $G_0 W_0$ approximation, yields

$$L^0_{(i_1 i_2)(i_3 i_4)} = -\mathrm{i} \frac{(f_{i_2} - f_{i_1})\delta_{i_1 i_3}\delta_{i_2 i_4}}{\epsilon_{i_2} - \epsilon_{i_1} - \omega - i\delta}, \tag{3.20}$$

where the Fermi-distribution f and the single-particle energies ϵ_{i_1} are introduced. Using this basis representation, the matrix Eq. (3.16) is expressed with an excitonic Hamiltonian H^e defined as

$$H^e_{(j_1 j_2)(j_3 j_4)} = (\epsilon_{j_2} - \epsilon_{j_1})\delta_{j_1 j_3}\delta_{j_2 j_4} - \mathrm{i}(f_{j_2} - f_{j_1})\Xi_{(j_1 j_2)(j_3 j_4)}, \tag{3.21}$$

and obtain

$$L_{(i_1 i_2)(i_3 i_4)}(\omega) = \mathrm{i}\left[H^e - \omega \right]^{-1}_{(i_1 i_2)(i_3 i_4)} (f_{i_4} - f_{i_3}). \tag{3.22}$$

4. Many-Body Approach to Core Excitations

4.1 Phenomenology of X-ray Absorption Fine Structure

X-ray absorption spectroscopy is the measurement of the energy-dependent absorption coefficient in the x-ray photon energy range. The absorption coefficient $\alpha(E)$ is defined by Beer's Law, which relates the incoming intensity of the x-ray beam I_0 and the transmitted intensity $I_t(z)$ behind a thickness z by

$$I_t(z) = e^{-\alpha(E)z} I_0. \qquad (4.1)$$

The schematic behavior of $\alpha(E)$ over a broad range of incident photon energy is displayed in Fig. (4.1). Three different features of the spectrum can be observed: Overall the absorption coefficient decreases with increasing photon energy.

Figure 4.1: Schematic view of x-range absorption spectroscopy over a broad energy range. Figure taken from Ref. [61].

This smooth decline is interrupted by sharp rises in the spectrum. These step-like features are called *absorption edges*. Lastly, small oscillations of the absorption coefficients occur at energies slightly above the absorption edges.
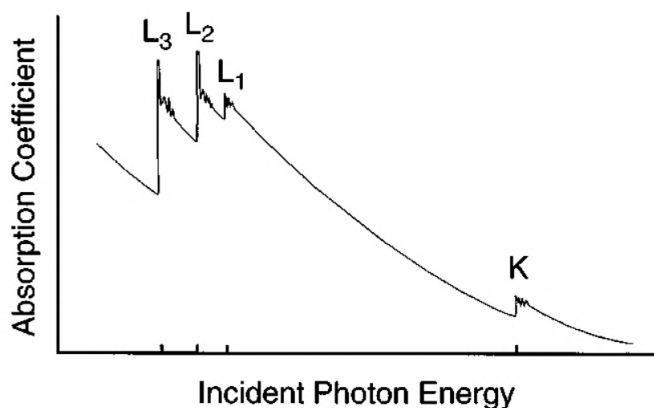
Absorption edge	Initial atomic state
K	$1s_{1/2}$
L_1	$2s_{1/2}$
$L_{2,3}$	$2p_{1/2}, 2p_{3/2}$
M_1	$3s_{1/2}$
$M_{2,3}$	$3p_{1/2}, 3p_{3/2}$
$M_{4,5}$	$3d_{3/2}, 3d_{5/2}$

Table 4.1: *Notation for x-ray absorption edges. Initial core states are described in the Russell-Saunders notation.*

These features are due to different processes happening in the material upon radiation with x-ray beams: The overall decrease of the absorption is due to the well-known background absorption of the atoms. The absorption edges are due to transitions of inner-shell electrons to the unoccupied states. Absorption edges are denoted by the inital atomic states in the transition. The notation for the nine edges representing transitions from the deepest core states are shown in table (4.1). The oscillations above the absorption edges are called *x-ray absorption fine structure* (XAFS). The XAFS is usually separated in two different regions: The x-ray absorption near-edge structure (XANES)[1], usually a region up to 40 eV beyond the absorption edge, and extended x-ray absorption fine structure (EXFAS), the region beyond the XANES. The EXFAS energy window can include a few hundred eV beyond the absorption edge, depending on the scale of the oscillations beyond the edge. The EXFAS is produced by transitions of the core electron to continous unoccupied states. It reveals the local geometrical structure of the sample [61]. The XANES

---

[1]XANES is sometimes also called near-edge x-ray absorption fine structure (NEXFAS)

represents transitions to bound unoccupied states and contains information on the local electronic and chemical structure of the absorbing atom [63]. In this work, focus lies on the calculation of XANES spectra for a given material and absorption edge.

4.2 Treatment of Core States

An accurate treatment of the inner-shell electrons in an all-electron calculation needs to take into account relativistic effects. Relativistic corrections including the spin-orbit splitting can be obtained *ab initio*, if electron energies and wavefunctions are determined by the Dirac equation. Since core electrons are tightly bound and, as such, strongly localized around the nuclear positions, the respective potentials are assumed to be spherically symmetric. The full Dirac equation can then be transformed into a set of coupled radial equations, similar to the case of the radial Schrödinger equation. The fact, that the Dirac Hamiltonian commutes with the total angular momentum operator $\hat{\mathbf{J}} = \hat{\mathbf{L}} + \hat{\mathbf{S}}$, is used to divide the Dirac equation into radial and spherical part. Eigenfunctions to $\mathbf{J}^2$ and J_z are constructed from the eigenvectors to $\mathbf{S}^2$ and S_z, which are the two-dimensional spinors, and the eigenvectors of $\mathbf{L}^2$ and L_z, which are the spherical harmonics. The resulting spin spherical harmonics $\Omega_{(l,s)j,M}$ have the form:

$$\Omega_{(l,\frac{1}{2})l+\frac{1}{2},M}(\hat{r}) = \begin{pmatrix} \sqrt{\frac{l+M+\frac{1}{2}}{2l+1}} Y_{l,M-\frac{1}{2}}(\hat{r}) \\ \sqrt{\frac{l-M+\frac{1}{2}}{2l+1}} Y_{l,M+\frac{1}{2}}(\hat{r}) \end{pmatrix}, \tag{4.2}$$

and

$$\Omega_{(l,\frac{1}{2})l-\frac{1}{2},M}(\hat{r}) = \begin{pmatrix} -\sqrt{\frac{l-M+\frac{1}{2}}{2l+1}} Y_{l,M-\frac{1}{2}}(\hat{r}) \\ \sqrt{\frac{l+M+\frac{1}{2}}{2l+1}} Y_{l,M+\frac{1}{2}}(\hat{r}) \end{pmatrix}.$$

With these eigenfunctions, the 4-component Dirac wavefunction is written as [32]:

$$\psi_{\kappa,M}(\mathbf{r}) = \begin{pmatrix} u_\kappa(r)\Omega_{\kappa,M}(\hat{\mathbf{r}}) \\ -iv_\kappa(r)\Omega_{-\kappa,M}(\hat{\mathbf{r}}) \end{pmatrix}, \tag{4.3}$$

where the quantum number κ is introduced, which is a unique index for a state $(l,s)j,M$:

$$\kappa = \begin{cases} -l-1 & \text{for } J = l + \frac{1}{2} \\ l & \text{for } J = l - \frac{1}{2} \end{cases}. \tag{4.4}$$

Hence, the wavefunctions $\psi_{\kappa,M}$ in Eq. (4.3) are four-component Dirac vectors, composed of two two-component spinors $\Omega_{\kappa,M}$, where the radial function of the large component is $u_\kappa(r)$ and that of the small component is $-iv_\kappa$. The radial functions are given by the coupled radial Dirac equations [81]:

$$\frac{\partial u_\kappa}{\partial r} = \frac{1}{c}(v_{eff}^s - \epsilon_\kappa)v_\kappa + \left(\frac{\kappa-1}{r}\right)u_\kappa \tag{4.5a}$$

$$\frac{\partial v_\kappa}{\partial r} = -\frac{\kappa+1}{r}v_\kappa + 2c\left(1 + \frac{1}{2c^2}(\epsilon_\kappa - v_{eff}^s)\right). \tag{4.5b}$$

A full derivation of the radial Dirac equation can be found in Refs. [81] and [31]. In order to calculate matrix elements with the non-relativistic states in the conduction band,

the small component of the core states was neglected, thereby producing spinor solutions $\psi_{\kappa,M}(\mathbf{r})$ for a given atom α at position $\mathbf{R}_\alpha$. This approximation is necessary, since the conduction states are solutions of the scalar-relativistic Hamiltonian and therefore the small component of these states is not accessible. This approximation to the Dirac core states are common in full-potential packages [see for example Ref. [7]]. The core wavefunction then takes the form

$$\psi_{\kappa,M}(\mathbf{r}) = \begin{cases} u_\kappa(r)\Omega_{\kappa,M}(\hat{\mathbf{r}}) & \text{for } r_\alpha \leq R_{MT} \\ 0 & \text{else} \end{cases}. \tag{4.6}$$

In the following a shorter notation of the core quantum numbers is introduced, contracting a set of (κ, M) quantum numbers into one index μ. This way, core radial function are denoted by $u_\mu^{\mathbf{k}}(r)$, with $\mu = (\kappa, M)$.

4.3 Treatment of Conduction States

Within the all-electron approach, conduction states (as well as valence states) are determined by a full-potential DFT calculation using a linearized augmented planewave (L)APW+LO basis set. In order to take relativistic effects within the MT spheres into account, the conduction states are treated in the zero-order regular approximation (ZORA) [41] to the Dirac equation without the spin-orbit coupling term. Thus, the Kohn-Sham Hamiltonian within the MT spheres for this states is written as

$$h^{ZORA} = \mathbf{p}\frac{1}{1 - \frac{v_{eff}^s}{2c^2}}\mathbf{p} + v_{eff}, \tag{4.7}$$

where v_{eff} is the full effective potential and v_{eff}^s its spherical average. For the many-body calculations the Kohn-Sham states $\psi_{i\mathbf{k}}(\mathbf{r})$ in the MT sphere of atom α are expanded in the basis of spherical harmonics:

$$\psi_{i\mathbf{k}}^\alpha(\mathbf{r}) = \sum_{lm} u_{lm}^{i\mathbf{k}}(r_\alpha)Y_{lm}(\hat{\mathbf{r}}_\alpha), \tag{4.8}$$

where the radial function is given in the (L)APW+LO basis as

$$\begin{aligned} u_{lm}^{i\mathbf{k}}(r_\alpha) = &\sum_{\mathbf{G}} c_{i\mathbf{G}}^{\mathbf{k}}\left[A_{lm\alpha}^{\mathbf{G}+\mathbf{k}}u_{l\alpha}(r_\alpha; \epsilon_{l\alpha}) + B_{lm\alpha}^{\mathbf{G}+\mathbf{k}}\dot{u}_{l\alpha}(r_\alpha; \epsilon_{l\alpha}) \right] \\ &+ \sum_\mu c_{i\mu}^{\mathbf{k}}\delta_{\alpha\alpha_\mu}\delta_{ll_\mu}\delta_{mm_\mu}\left[a_\mu u_{l\alpha}(r_\alpha; \epsilon_{l\alpha}) + b_\mu\dot{u}_{l\alpha}(r_\alpha; \epsilon_{l\alpha}) \right]. \end{aligned} \tag{4.9}$$

The `exciting` package uses a flexible basis set, allowing LAPW+LO and APW+LO basis set (compare Chapter 2.3) and even basis sets with higher derivatives of the radial basis functions [23]. While APW+LO is obtained from Eq. (4.9) with $B_{lm\alpha}^{\mathbf{G}+\mathbf{k}} = 0$, it is stressed that the description in Eq. (4.8) is more general, and allows for all possible basis descriptions in the package `exciting`. In order to calculate matrix elements between the spinorial core states and the conduction states, an approximation for the spinor character of the conduction state is necessary. Here, the states are assumed to take the form

$$\psi_{spinor}^{i\mathbf{k}}(\mathbf{r}) = \begin{pmatrix} \frac{1}{\sqrt{2}} \\ \frac{1}{\sqrt{2}} \end{pmatrix}\psi^{i\mathbf{k}}(\mathbf{r}), \tag{4.10}$$

thereby representing an average contribution between the two spin-channels. With this approximation to the spinorial character of the conduction states, spin-unpolarized DFT calculations can be used as a starting point for the XAS calculations.

4.4 Effective Hamiltonian

As seen in Chapter 3.3, the two-particle correlation function can be expressed in terms of an excitonic Hamiltonian (see Eq. (3.21)). This excitonic Hamiltonian as expressed in Eq. (3.21) can be simplified, considering the nature of the transitions in x-ray spectroscopy: All transition occur from fully occupied core states c ($f_c = 1$) to unoccupied conduction states u ($f_u = 0$). These two groups of states are separated by a wide energy gap [1]. Inserting these Fermi-distrubutions yields a reduced excitonic Hamiltonian of the form

$$H^e = \begin{pmatrix} H^e_{c_1u_1\mathbf{k1},c_2u_2\mathbf{k2}} & H^e_{c_1u_1\mathbf{k1},u_2c_2\mathbf{k2}} \\ H^e_{u_1c_1\mathbf{k_1},c_2u_2\mathbf{k_2}} & H^e_{u_1c_1\mathbf{k_1},u_2c_2\mathbf{k_2}} \end{pmatrix}. \tag{4.11}$$

The Hamiltonian in Eq. (3.21) has the size $(N_u + N_c)^4 N_k^4$ for N_u unoccupied states, N_c core states, and N_k k-points, whereas the reduced Hamiltonian in Eq. (4.11) has the size $N_c^4 N_u^4 N_k^4$. The block matrices of the effetive Hamiltonian can be written as:

$$H^e_{c_1u_1\mathbf{k1},c_2u_2\mathbf{k_2}} = (\epsilon_{u_1\mathbf{k_1}} - \epsilon_{c_1})\delta_{c_1c_2}\delta_{u_1u_2} + \mathrm{i}\Xi_{c_1u_1\mathbf{k1},c_2u_2\mathbf{k2}} \tag{4.12a}$$

$$H^e_{c_1u_1\mathbf{k1},u_2c_2\mathbf{k_2}} = +\mathrm{i}\Xi_{c_1u_1\mathbf{k_1},u_2c_2\mathbf{k_2}} \tag{4.12b}$$

$$H^e_{u_1c_1\mathbf{k1},c_2u_2\mathbf{k_2}} = -\left[H^e_{c_1u_1\mathbf{k_1},u_2c_2\mathbf{k_2}}\right]^* \tag{4.12c}$$

$$H^e_{u_1c_1\mathbf{k1},u_2c_2\mathbf{k_2}} = -\left[H^e_{c_1u_1\mathbf{k1},c_2u_2\mathbf{k_2}}\right]^*. \tag{4.12d}$$

The matrix size can be furthermore reduced by the Tamm-Dancoff approximation: If the coupling in the off-diagonal blocks (Eqs. (4.12b) and (4.12c)) can be neglected, only the first block has to be calculated, since the matrix takes block-diagonal form and eigenvalues and -vectors of Eq. (4.12a) uniquely define the eigenvalues and -vectors of Eq. (4.12d). Thus, the matrix size is reduced to $N_u^2 N_c^2 N_k^2$. It has been shown [59] that the Tamm-Dancoff approximation in the optical limit is justified if the binding energies of the excitations are small compared to the band gap. For calculations at finite momentum transfer the approximation breaks down even if the binding energies are small [66]. Since in this work, x-ray spectroscopy is considered in the optical limit, where the band gap between the core states and the conduction band is typically several hundred eV, whereas binding energies are in the range of few eV, the Tamm-Dancoff approximation is valid. Using the spectral theorem, the correlation function can now be expressed in the eigenvalues E^λ and eigenstates $A^\lambda_{cu\mathbf{k}}$ of the Hamiltonian in Eq. (4.12a):

$$L_{c_1u_1\mathbf{k_1},c_2u_2\mathbf{k_2}} = -\mathrm{i}\sum_\lambda \frac{A^\lambda_{c_1u_1\mathbf{k_1}}\left[A^\lambda_{c_2u_2\mathbf{k_2}}\right]^*}{E^\lambda - \omega}. \tag{4.13}$$

The eigenvalue problem is expressed as

$$\sum_{c'u'\mathbf{k}'} H^{BSE}_{cu\mathbf{k},c'u'\mathbf{k}'} A^\lambda_{c'u'\mathbf{k}'} = E^\lambda A^\lambda_{cu\mathbf{k}}, \tag{4.14}$$

where the eigenvectors $A^\lambda_{cu\mathbf{k}}$ are the expansion coefficients of the excitonic wavefunction $\Phi^\lambda(\mathbf{r}, \mathbf{r}')$ with transition energy E^λ in the single-particle wavefunctions:

$$\Phi^\lambda(\mathbf{r}_e, \mathbf{r}_h) = \sum_{cu\mathbf{k}} A^\lambda_{cu\mathbf{k}} \psi_{u\mathbf{k}}(\mathbf{r}_e)\psi_{c\mathbf{k}}(\mathbf{r}_h). \tag{4.15}$$

---

[1]The original derivation in Ref. [58] for the case of optical spectroscopy was limited to insulators and semiconductors to ensure that the two groups of states are separated by an energy gap. For x-ray spectroscopy, calculations are possible for metals as well.

Here, $\mathbf{r}_e$ is the position of the excited electron and $\mathbf{r}_h$ the position of the core hole. The transition coefficients t_λ are obtained as

$$t_\lambda = \sum_{cu\mathbf{k}} A^\lambda_{cu\mathbf{k}} \frac{\langle c\mathbf{k}|\hat{\mathbf{p}}|u\mathbf{k}\rangle}{\epsilon_{u\mathbf{k}} - \epsilon_c}, \tag{4.16}$$

where $\epsilon_{u\mathbf{k}}$ is the single-particle energy of the conduction state, and ϵ_c the single-particle energy of the core state. $\langle c\mathbf{k}|\hat{\mathbf{p}}|u\mathbf{k}\rangle$ are the momentum-matrix elements between the two states. Using these transition coefficients, the imaginary part of the dielectric tensor is obtained as

$$\text{Im } \epsilon_M(\omega) = \frac{8\pi^2}{\Omega} \sum_\lambda |t_\lambda|^2 \delta(\omega - E^\lambda). \tag{4.17}$$

The effective Hamiltonian H^{BSE} is obtained from Eq. (4.12a)

$$H^{BSE}_{cu\mathbf{k},c'u'\mathbf{k}'} = (\epsilon_{u\mathbf{k}} - \epsilon_c)\delta_{cc'}\delta_{uu'} + \mathrm{i}\Xi_{cu\mathbf{k},c'u'\mathbf{k}'}, \tag{4.18}$$

using the interaction kernel $\Xi_{cu\mathbf{k},c'u'\mathbf{k}'}$, defined in eq. (3.15):

$$\Xi_{cu\mathbf{k},c'u'\mathbf{k}'} = \int d^3r_1 d^3r'_1 d^3r_2 d^3r'_2 \psi_{i1}(\mathbf{r}_1)\psi^*_{i2}(\mathbf{r}'_1)\psi^*_{i3}(\mathbf{r}_2)\psi_{i4}(\mathbf{r}'_2)\Xi(\mathbf{r}_1, \mathbf{r}'_1, \mathbf{r}_2, \mathbf{r}'_2) \tag{4.19}$$

In Chapter 3, the two-particle correlation function was expanded in single-particle wave-functions $\psi_{i1}(\mathbf{r})$ without specifying the spin characters of these states. Since spinorial states are used in this work in order to include the spin-orbit coupling of the core states explicitly, in the following the spin index $\sigma = 1, 2$ for spin-up and spin-down components is introduced. Since the Coulomb interaction is diagonal in the spinor space, the derivation in Chapter 2 is independent of the character of the wavefunctions.

The effective BSE Hamiltonian H^{BSE} can be separated in three contributions:

$$H^{BSE} = H^{diag} + H^x + H^c, \tag{4.20}$$

where H^{diag} is the diagonal contribution

$$H^{diag}_{cu\mathbf{k},c'u'\mathbf{k}'} = (\epsilon_{u\mathbf{k}} - \epsilon_c)\delta_{cc'}\delta_{uu'}\delta_{\mathbf{k}\mathbf{k}'}. \tag{4.21}$$

H^x is the repulsive exchange part

$$H^x_{cu\mathbf{k},c'u'\mathbf{k}'} = \int d^3r d^3r' \sum_\sigma \psi_{c\mathbf{k}\sigma}(\mathbf{r})\psi^*_{u\mathbf{k}\sigma}(\mathbf{r})\bar{v}(\mathbf{r}, \mathbf{r}') \sum_{\sigma'} \psi^*_{c'\mathbf{k}'\sigma'}(\mathbf{r}')\psi_{u'\mathbf{k}'\sigma'}(\mathbf{r}') \tag{4.22}$$

using $\bar{v}(\mathbf{r}, \mathbf{r}')$ as the short-range part of the bare Coulomb potential. H_c is the attractive direct part

$$H^c_{cu\mathbf{k},c'u'\mathbf{k}'} = -\int d^3r d^3r' \sum_\sigma \psi_{c\mathbf{k}\sigma}(\mathbf{r})\psi^*_{c'\mathbf{k}'\sigma}(\mathbf{r})W(\mathbf{r}, \mathbf{r}') \sum_{\sigma'} \psi^*_{u\mathbf{k}\sigma'}(\mathbf{r}')\psi_{u'\mathbf{k}'\sigma'}(\mathbf{r}'), \tag{4.23}$$

where $W(\mathbf{r}, \mathbf{r}')$ is the statically screened Coulomb interaction of the system.

4.5 Direct and Exchange Interaction

The direct and exchange terms in Eq. (4.22) and (4.23) are evaluated the easiest by inserting the reciprocal representation of the bare and screened Coulomb interaction. Using

the Fourier components $\bar{v}_{\mathbf{G}}(\mathbf{q})$ of the bare Coulomb potential, the exchange interaction of Eq. (3.18) takes the form

$$H^x_{cu\mathbf{k},c'u'\mathbf{k}'} = \frac{1}{V} \sum_{\mathbf{G}} M^*_{cu\mathbf{k}}(\mathbf{G}) \bar{v}_{\mathbf{G}}(\mathbf{q} = 0) M_{c'u'\mathbf{k}'}(\mathbf{G}), \qquad (4.24)$$

where V is the volume of the unit cell. Here the planewave matrix elements $M_{cu\mathbf{k}}(\mathbf{q}+\mathbf{G})$ is introduced, defined as

$$M_{nm\mathbf{k}}(\mathbf{q} + \mathbf{G}) = \sum_{\sigma} \langle \psi_{n\mathbf{k}\sigma} | \exp(-i(\mathbf{q} + \mathbf{G})) | \psi_{m(\mathbf{k}+\mathbf{q})\sigma} \rangle. \qquad (4.25)$$

Analogously, the Fourier components $W_{\mathbf{GG}'}(\mathbf{q})$, with $\mathbf{q} = \mathbf{k}' - \mathbf{k}$, can be used to express the direct interaction of Eq. (3.20) as

$$H^c_{cu\mathbf{k},c'u'\mathbf{k}'} = -\frac{1}{V} \sum_{\mathbf{GG}'} M^*_{cc'\mathbf{k}}(\mathbf{q} + \mathbf{G}) W_{\mathbf{GG}'}(\mathbf{q}) M^*_{uu'\mathbf{k}}(\mathbf{q} + \mathbf{G}'). \qquad (4.26)$$

The Fourier components of the screened Coulomb interaction are calculated using the inverse microscopic dielectric tensor $\epsilon^{-1}_{\mathbf{GG}'}(\mathbf{q})$. Using only the $\omega = 0$ contribution (static screening), the screened Coulomb interaction is expressed as

$$W_{\mathbf{GG}'}(\mathbf{q}) = \frac{4\pi \epsilon^{-1}_{\mathbf{GG}'}}{|\mathbf{q} + \mathbf{G}||\mathbf{q} + \mathbf{G}'|}. \qquad (4.27)$$

The microscopic dielectric tensor is obtained as

$$\epsilon_{\mathbf{GG}'}(\mathbf{q}) = \delta_{\mathbf{GG}'} - \frac{4\pi}{|\mathbf{q} + \mathbf{G}||\mathbf{q} + \mathbf{G}'|} \hat{P}^0_{\mathbf{GG}'}(\mathbf{q}), \qquad (4.28)$$

where the irreducible polarization in the random-phase approximation (RPA) is

$$\hat{P}^0_{\mathbf{GG}'}(\mathbf{q}) = \frac{4\pi}{\Omega} \sum_{cv\mathbf{k}} \frac{M_{cv\mathbf{k}}(\mathbf{q} + \mathbf{G})[M_{cv\mathbf{k}}(\mathbf{q} + \mathbf{G}')]^*}{\epsilon_{v\mathbf{k}} - \epsilon_{c\mathbf{k}}}. \qquad (4.29)$$

Although transitions occur between the core states and unoccupied states, the summation in Eq. (4.29) inlcudes transitions between all states, i.e. also valence states contribute to the screening.

4.6 Matrix Elements

Since both the conduction states in the muffin-tin spheres within the LAPW+LO description of Eq. (4.10), and the core states in Eq. (4.6) are localized, Bloch states $\phi_{n\alpha\mathbf{k}}$ have to be constructed from the localized states[2] $\psi_{n\alpha\mathbf{k}}$ defined in the MT sphere of the atom α:

$$\phi_{n\alpha\mathbf{k}}(\mathbf{r}) = \sum_{\mathbf{R}} \psi_{n\alpha\mathbf{k}}(\mathbf{r}_\alpha - \mathbf{R}) e^{i\mathbf{k}\mathbf{R}}, \qquad (4.30)$$

where $\mathbf{R}$ is a lattice vector of the crystal and $\mathbf{r}_\alpha = \mathbf{r} - \mathbf{R}_\alpha$. The resulting states obey the Bloch theorem, i.e. $\phi_{n\alpha\mathbf{k}}(\mathbf{r} + \mathbf{R}) = e^{i\mathbf{k}\mathbf{R}}\phi_{n\alpha\mathbf{k}}(\mathbf{r})$. In the following, it is shown that

---

[2]Note that while the core state have no dependence on the wavevector $\mathbf{k}$, even the localized conduction states in the MT spheres depend on the wavevector through the augmentation of the planewaves in the interstitial region.

matrix elements can be obtained by an integration over the unit cell volume instead of the whole crystal volume. This proof is valid for a given set of states $\psi_{n\alpha\mathbf{k}}$ that do not obey the Bloch condition, such that it is not specified here whether the states are core or conduction states.

A matrix element for a given local operator $\hat{A}(\mathbf{r})$ is given as

$$\langle \phi_{n\alpha\mathbf{k}}|\hat{A}|\phi_{m\alpha\mathbf{k}'}\rangle = \int_{\Omega} d^3 r\, \phi_{n\alpha\mathbf{k}}^*(\mathbf{r})\hat{A}(\mathbf{r})\phi_{m\alpha\mathbf{k}'}(\mathbf{r}), \tag{4.31}$$

where Ω is the volume of the entire crystal. Using Eq. (4.30), this is now expressed as:

$$\langle \phi_{n\alpha\mathbf{k}}|\hat{A}|\phi_{m\alpha\mathbf{k}'}\rangle = \sum_{\mathbf{R}}\sum_{\mathbf{R}'} e^{-i\mathbf{k}\mathbf{R}}e^{i\mathbf{k}'\mathbf{R}'}\int_{\Omega} d^3 r\, \psi_{n\alpha\mathbf{k}}^*(\mathbf{r}_\alpha - \mathbf{R})\hat{A}(\mathbf{r})\psi_{m\alpha\mathbf{k}'}(\mathbf{r}_\alpha - \mathbf{R}') \tag{4.32}$$

$$= \sum_{\mathbf{R}}\sum_{\mathbf{R}'} e^{i(\mathbf{k}'-\mathbf{k})\mathbf{R}}e^{i(\mathbf{R}'-\mathbf{R})\mathbf{k}}\int_{\Omega} d^3 r\, \psi_{n\alpha\mathbf{k}}^*(\mathbf{r}_\alpha - \mathbf{R})\hat{A}(\mathbf{r})\psi_{m\alpha\mathbf{k}'}(\mathbf{r}_\alpha - \mathbf{R}').$$

This equation can be rewritten, since $\mathbf{R}'' = \mathbf{R} - \mathbf{R}'$ is also a lattice vector of the crystal. One obtains

$$\langle \phi_{n\alpha\mathbf{k}}|\hat{A}|\phi_{m\alpha\mathbf{k}'}\rangle = \sum_{\mathbf{R}'}\sum_{\mathbf{R}''} e^{i(\mathbf{k}'-\mathbf{k})\mathbf{R}'}e^{i\mathbf{k}\mathbf{R}''}\int_{\Omega} d^3 r\, \psi_{n\alpha\mathbf{k}}^*(\mathbf{r}_\alpha)\hat{A}(\mathbf{r}+\mathbf{R})\psi_{m\alpha\mathbf{k}'}(\mathbf{r}_\alpha - \mathbf{R}''). \tag{4.33}$$

Since the functions are centered at one atom α, the integral vanishes for all non-zero $\mathbf{R}''$, and the integral can now be reduced from the entire crystal volume Ω to the unit cell volume Ω_0:

$$\langle \phi_{n\alpha\mathbf{k}}|\hat{A}|\phi_{m\alpha\mathbf{k}'}\rangle = \sum_{\mathbf{R}'} e^{i(\mathbf{k}'-\mathbf{k})\mathbf{R}''}\int_{\Omega_0} d^3 r\, \psi_{n\alpha\mathbf{k}}^*(\mathbf{r}_\alpha)\hat{A}(\mathbf{r}+\mathbf{R})\psi_{m\alpha\mathbf{k}'}(\mathbf{r}_\alpha). \tag{4.34}$$

The translational symmetry of the operator $\hat{A}$ has to be considered now: If the operator obeys the full translational symmetry of the crystal, i.e. $\hat{A}(\mathbf{r}+\mathbf{R}) = \hat{A}(\mathbf{r})$, the matrix element is

$$\langle \phi_{n\alpha\mathbf{k}}|\hat{A}|\psi_{m\alpha\mathbf{k}'}\rangle = \sum_{\mathbf{R}'} e^{i(\mathbf{k}'-\mathbf{k})\mathbf{R}''}\int_{\Omega_0} d^3 r\, \psi_{n\alpha\mathbf{k}}^*(\mathbf{r}_\alpha)\hat{A}(\mathbf{r})\psi_{m\alpha\mathbf{k}'}(\mathbf{r}_\alpha). \tag{4.35}$$

Using this identity

$$\sum_{\mathbf{R}} e^{i\mathbf{q}\mathbf{R}} = \frac{\Omega}{\Omega_0}\sum_{\mathbf{G}} \delta_{\mathbf{q},\mathbf{G}}, \tag{4.36}$$

where $\mathbf{G}$ are the reciprocal lattice vectors, one obtains

$$\langle \phi_{n\alpha\mathbf{k}}|\hat{A}|\phi_{m\alpha\mathbf{k}'}\rangle = \frac{\Omega}{\Omega_0}\delta_{\mathbf{k},\mathbf{k}'}\int_{\Omega_0} d^3 r\, \psi_{n\alpha\mathbf{k}}^*(\mathbf{r}_\alpha)\hat{A}(\mathbf{r}_\alpha)\psi_{m\alpha\mathbf{k}'}(\mathbf{r}_\alpha) \tag{4.37}$$

$$= \frac{\Omega}{\Omega_0}\langle \psi_{n\alpha\mathbf{k}}|\hat{A}|\psi_{m\alpha\mathbf{k}}\rangle_{\Omega_0}.$$

Here the fact is used that both $\mathbf{k}$ and $\mathbf{k}'$ are vectors from the first Brillouin zone. One sees that for these operators, the calculation of expectation values between to Bloch states can be reduced to expectation values in one unit-cell for states with the same $\mathbf{k}$-vectors. Such operators therefore obey momentum conservation.

Different results are obtained for operators that obey the Bloch condition as

$$\hat{B}_\mathbf{q}(\mathbf{r}+\mathbf{R}) = e^{i(\mathbf{q}+\mathbf{G})\mathbf{R}}\hat{B}_\mathbf{q}(\mathbf{r}). \tag{4.38}$$

For these operator, Eq. (4.34) can be written as

$$\langle \phi_{n\alpha\mathbf{k}} | \hat{B}_{\mathbf{q}}(\mathbf{r}) | \phi_{m\alpha\mathbf{k}'} \rangle = \sum_{\mathbf{R}'} e^{i(\mathbf{k}'-\mathbf{k}-\mathbf{q}-\mathbf{G})\mathbf{R}''} \int_{\Omega_0} d^3 r \psi_{n\alpha\mathbf{k}}^*(\mathbf{r}_\alpha) \hat{B}_{\mathbf{q}}(\mathbf{r}) \psi_{m\alpha\mathbf{k}'}(\mathbf{r}_\alpha). \quad (4.39)$$

Using the identity, Eq. (4.36), one can now write

$$\sum_{\mathbf{R}'} e^{i(\mathbf{k}'-\mathbf{k}-\mathbf{q}-\mathbf{G})\mathbf{R}''} = \frac{\Omega}{\Omega_0} \sum_{\mathbf{G}'} \delta_{\mathbf{k}'-\mathbf{k}-\mathbf{q}-\mathbf{G},\mathbf{G}'} = \frac{\Omega}{\Omega_0} \delta_{\mathbf{k}',\mathbf{k}+\mathbf{q}}, \quad (4.40)$$

and therefore

$$\langle \phi_{n\alpha\mathbf{k}} | \hat{B}_{\mathbf{q}}(\mathbf{r}) | \phi_{m\alpha\mathbf{k}'} \rangle = \frac{\Omega}{\Omega_0} \int_{\Omega_0} d^3 r \psi_{n\alpha\mathbf{k}}^*(\mathbf{r}_\alpha) \hat{B}_{\mathbf{q}}(\mathbf{r}) \psi_{m\alpha(\mathbf{k}+\mathbf{q})}(\mathbf{r}_\alpha) \quad (4.41)$$

$$= \frac{\Omega}{\Omega_0} \langle \psi_{n\alpha\mathbf{k}} | \hat{B}_{\mathbf{q}}(\mathbf{r}) | \psi_{m\alpha(\mathbf{k}+\mathbf{q})} \rangle_{\Omega_0}.$$

For these operators, expectation values can also be calculated in the first Brillouin zone, where only states that obey $\mathbf{k}' = \mathbf{k} + \mathbf{q}$ contribute.

4.7 Atomic Separation of the BSE Hamiltonian

In x-ray spectroscopy the BSE Hamiltonian can be separated in atomic contributions. This reduces the size of the matrix equation that has to be diagonalized. In the following this separation is provided for a system with two atoms labeled α and β, but the extension to an arbitrary number of atoms is straightforward.

Using the definition of core states in Eq. (4.6), one obtains:

$$\begin{aligned} \mathbf{r}_\alpha &< \mathbf{R}_{MT}: \psi_{c'\mathbf{k}'}(\mathbf{r}) = 0 \\ \mathbf{r}_\beta &< \mathbf{R}_{MT}: \psi_{c\mathbf{k}}(\mathbf{r}) = 0 \\ \mathbf{r} &\in I: \psi_{c\mathbf{k}}(\mathbf{r}) = \psi_{c'\mathbf{k}'}(\mathbf{r}) = 0 \end{aligned} \quad . \quad (4.42)$$

It follows that

$$H_{c u \mathbf{k}, c' u' \mathbf{k}'}^x = H_{c u \mathbf{k}, c' u' \mathbf{k}'}^c = 0 \text{ for } c \in \alpha \text{ and } c' \in \beta. \quad (4.43)$$

The full Hamiltonian $H_{c u \mathbf{k}, c' u' \mathbf{k}'}^{BSE}$ has the size $(N_{c_1} + N_{c_2})^2 N_u^2 N_k^2$, where N_{c_1} and N_{c_2} are the number of core states at atom α and β respectivly, N_u the number of unoccupied states and N_k the number of $\mathbf{k}$-points. The Hamiltonian is now written in block form as

$$H^{BSE} = \begin{pmatrix} H_{c_1 u \mathbf{k}, c_1' u' \mathbf{k}'}^{BSE} & H_{c_1 u \mathbf{k}, c_2' u' \mathbf{k}'}^{BSE} \\ H_{c_2 u \mathbf{k}, c_1' u' \mathbf{k}'}^{BSE} & H_{c_1 u \mathbf{k}, c_2' u' \mathbf{k}'}^{BSE} \end{pmatrix} \quad (4.44)$$

Inserting 4.43, the full Hamiltonian H^{BSE} assumes a block diagonal form, with the block matrices H_α^{BSE} and H_β^{BSE}:

$$H^{BSE} = \begin{pmatrix} H_\alpha^{BSE} & 0 \\ 0 & H_\beta^{BSE} \end{pmatrix}. \quad (4.45)$$

Using the eigenstates of the block matrices B^λ and $C^{\lambda'}$, which obey $H_\alpha^{BSE} B^\lambda = E^\lambda B^\lambda$ and $H_\beta^{BSE} C^{\lambda''} = E^{\lambda''} C^{\lambda''}$ respectivily, the eigenstates of H^{BSE} become:

$$A^\lambda = \left\{ \begin{pmatrix} B^{\lambda'} \\ 0 \end{pmatrix}, \begin{pmatrix} 0 \\ C^{\lambda''} \end{pmatrix} \right\}. \quad (4.46)$$

The imaginary part of the macroscopic dielectric function defined in Eq. (4.16) and (4.17) is thus

$$\mathrm{Im}\,\epsilon_M(\omega) = \frac{8\pi^2}{\Omega} \sum_\lambda \left| \sum_{cu\mathbf{k}} A^\lambda_{cu\mathbf{k}} \frac{\langle c\mathbf{k}|\hat{\mathbf{p}}|u\mathbf{k}\rangle}{\epsilon_{u\mathbf{k}} - \epsilon_c} \right|^2 \delta(\omega - E^\lambda), \tag{4.47}$$

and since the eigenvalues $B^{\lambda'}$ and $C^{\lambda''}$ are fully decoupled, one finally obtains

$$\sum_\lambda \left| \sum_{cu\mathbf{k}} A^\lambda_{cu\mathbf{k}} \frac{\langle c\mathbf{k}|\hat{\mathbf{p}}|u\mathbf{k}\rangle}{\epsilon_{u\mathbf{k}} - \epsilon_c} \right|^2 = \sum_{\lambda'} \left| \sum_{cu\mathbf{k}} B^{\lambda'}_{cu\mathbf{k}} \frac{\langle c\mathbf{k}|\hat{\mathbf{p}}|u\mathbf{k}\rangle}{\epsilon_{u\mathbf{k}} - \epsilon_c} \right|^2 + \sum_{\lambda''} \left| \sum_{cu\mathbf{k}} C^{\lambda''}_{cu\mathbf{k}} \frac{\langle c\mathbf{k}|\hat{\mathbf{p}}|u\mathbf{k}\rangle}{\epsilon_{u\mathbf{k}} - \epsilon_c} \right|^2 \tag{4.48}$$

With this, the macroscopic dielectric function $\mathrm{Im}\,\epsilon_M$ can be expressed as a sum of the independent contribution from the two atoms:

$$\mathrm{Im}\,\epsilon_M = \mathrm{Im}\,\epsilon_M^\alpha + \mathrm{Im}\,\epsilon_M^\beta, \tag{4.49}$$

where each of the contributions is calculated by taking only the core states of the respective atom into account. Therefore atomic indizes will be omitted in the following and it is assumed that the contribution to the dielectric function by individual atoms of the unit cell are calculated.

5. Implementation

The evaluation of matrix elements in the (L)APW+LO basis is computationally demanding, since the partitioning of real space leads to two expressions for any real space integral, separating atomic and interstitial contributions. Furthermore, matrix elements are often reformulated in terms of matrix elements between basis functions, such that multiplications of big matrices have to be employed. For the calculation of matrix elements between core states and conduction states, both of these difficulties can be avoided. Since the core states, as defined in Eq. (4.6), only live in the muffin-tin sphere of one atom, only this region of space has to be taken into account. In the following, only matrix elements for a given atom are considered and the atomic index α is dropped. The conduction states are also not expressed in the LAPW+LO basis, but rather in an expansion in spherical harmonics as in Eq. (4.10).

5.1 Spin Gaunt Coefficients

Gaunt coefficients are matrix elements of spherical harmonics in a basis of spherical harmonics, defined as:

$$C_{lml''m''}^{l'm'} = \langle Y_{l'm'}|Y_{lm}|Y_{l''m''}\rangle = \int d\Omega \; Y_{l'm'}^{\star}Y_{lm}Y_{l''m''} \tag{5.1}$$

Generalizing these coefficients to matrix elements of spherical harmonics between the spherical part of the core and conduction spinor states (see Chapters 4.2 and 4.3), the planewave elements can be expressed solely in scalar quantities. To make the following equations more concise, the notation for the spin spherical harmonics is introduced:

$$\Omega_{\mu}(\hat{r}) = \begin{pmatrix} a_1(\mu)Y_{lm_1}(\hat{r}) \\ a_2(\mu)Y_{lm_2}(\hat{r}) \end{pmatrix}, \tag{5.2}$$

where the prefactors $a(\mu)$ are defined as in Eq.(4.2), and the m-index in the spherical harmonics is $m_{1,2} = M \pm \frac{1}{2}$ as in Eq. (4.2).
In order to describe the spherical parts of the planewave matrix elements, three different kinds of spin Gaunt coefficients have to be considered:

Core-core spin Gaunt coefficients are defined as

$$C_{lm\mu''}^{\mu'} = \langle \Omega_{\mu'}|Y_{lm}|\Omega_{\mu''}\rangle \tag{5.3}$$

$$= \int d\Omega \left(a_1(\mu')a_1(\mu'')Y_{l'm_1'}^{\star}Y_{lm}Y_{l',m_1''} + a_2(\mu')a_2(\mu'')Y_{l'm_2'}^{\star}Y_{lm}Y_{l',m_2''}\right)$$

$$= a_1(\mu')a_1(\mu'')C_{lml''m_1''}^{l'm_1'} + a_2(\mu')a_2(\mu'')C_{lml''m_2''}^{l'm_2'}.$$

Conduction-core spin Gaunt coefficients are defined as

$$C_{lm\mu''}^{l'm'} = \langle \begin{pmatrix} \frac{1}{\sqrt{2}}Y_{l'm'} \\ \frac{1}{\sqrt{2}}Y_{l'm'} \end{pmatrix}|Y_{lm}|\Omega_{\mu''}\rangle \tag{5.4}$$

$$= \int d\Omega \left(\frac{1}{\sqrt{2}}a_1(\mu'')Y_{l'm'}^{\star}Y_{lm}Y_{l'',m_1''} + \frac{1}{\sqrt{2}}a_2(\mu'')Y_{l'm'}^{\star}Y_{lm}Y_{l'',m_2''}\right)$$

$$= \frac{1}{\sqrt{2}} a_1(\mu'') C^{l'm'}_{lml''m''_1} + \frac{1}{\sqrt{2}} a_2(\mu'') C^{l'm'}_{lml''m''_2}.$$

Core-conduction spin Gaunt coefficients are defined as

$$C^{\mu'}_{lm,l''m''} = \langle \Omega_{\mu'} | Y_{lm} | \begin{pmatrix} \frac{1}{\sqrt{2}} Y_{l''m''} \\ \frac{1}{\sqrt{2}} Y_{l''m''} \end{pmatrix} \rangle \tag{5.5}$$

$$= \int d\Omega \left(\frac{1}{\sqrt{2}} a_1(\mu') Y^\star_{l'm'_1} Y_{lm} Y_{l''m''} + \frac{1}{\sqrt{2}} a_2(\mu') Y^\star_{l'm'_2} Y_{lm} Y_{l''m''} \right)$$

$$= \frac{1}{\sqrt{2}} a_1(\mu') C^{l'm'_1}_{lml''_i m''} + a_2(\mu') C^{l'm'_2}_{lml''_i m''}$$

.

5.2 Momentum Matrix Elements

Momentum matrix elements are used to construct the dielectric tensor from the eigenvalues and -vectors of the BSE Hamiltonian. Matrix elements for core excitations have the form:

$$P^j_{\mu\mathbf{k},m\mathbf{k}'} = \langle \phi_{\mu\mathbf{k}} | \hat{p}j | \phi_{m\mathbf{k}'} \rangle. \tag{5.6}$$

As proved in Chapter 4.6, matrix elements can be evaluated using solely the localized wavefunctions $\psi_{m\mathbf{k}}$:

$$P^j_{\mu m\mathbf{k}} = \langle \psi_\mu | \hat{p}_j | \psi_{m\mathbf{k}} \rangle_{\Omega_0}. \tag{5.7}$$

The gradient of the radial wavefunction of a state $|\psi_{m\mathbf{k}}\rangle$ inside the muffin-tin sphere can be expressed in terms of spherical harmonics as:

$$\nabla_j \left[\sum_{l'm'} u^{i\mathbf{k}}_{l'm'}(r) Y_{l'm'}(\hat{r}) \right] = \sum_{l'm'} F^{ji\mathbf{k}}_{l'm'}.(r) Y_{l'm'}(\hat{r}) \tag{5.8}$$

Thus, the gradient of a function expanded in spherical harmonics is expanded in spherical harmonics as well. The matrix element $P^j_{\mu m\mathbf{k}}$ can then be written as:

$$P^j_{\mu m\mathbf{k}} = \sum_{l'm'} \int dr \left(r^2 u^\mu(r) F^{ji\mathbf{k}}_{l'm'}(r) \right) \int d\Omega \left(\Omega_\mu Y^*_{l'm'} \right) \tag{5.9}$$

$$= \frac{1}{\sqrt{2}} \left[a_1(\mu) \int dr \left(r^2 u^\mu(r) F^{ji\mathbf{k}}_{lm_1}(r) \right) + a_2(\mu) \int dr \left(r^2 u^\mu(r) F^{ji\mathbf{k}}_{lm_2}(r) \right) \right],$$

where the fact that

$$\int d\Omega \left(\Omega_\mu \cdot \begin{pmatrix} \frac{1}{\sqrt{2}} Y^\star_{l'm'} \\ \frac{1}{\sqrt{2}} Y^\star_{l'm'} \end{pmatrix} \right) = \delta_{ll'} \frac{1}{\sqrt{2}} (\delta_{m_1m'} + \delta_{m_2m'}) \tag{5.10}$$

was used.

5.3 Planewave Matrix Elements

The planewave matrix elements $M_{nm\mathbf{k}}(\mathbf{q} + \mathbf{G})$ are defined as

$$M_{nm\mathbf{kk'}}(\mathbf{q} + \mathbf{G}) = \langle \phi_{n\mathbf{k}} | \exp(-i(\mathbf{q} + \mathbf{G})) | \phi_{m(\mathbf{k'})} \rangle. \qquad (5.11)$$

Using 4.41, these matrix elements are expressed in localized wavefunctions as

$$M_{nm\mathbf{k}}(\mathbf{q} + \mathbf{G}) = < \psi_{n\mathbf{k}} | \exp(-i(\mathbf{q} + \mathbf{G})) | \psi_{m(\mathbf{k+q})} >_{\Omega_0}. \qquad (5.12)$$

In order to evaluate these elements in the muffin-tin spheres, where a planewave description of the states does not exist, the expansion of planewaves in terms of spherical harmonics Y_{lm} and Bessel functions j_l is employed:

$$\mathrm{e}^{-i\mathbf{qr}} = 4\pi \sum_{lm} (-i)^l j_l(qr) Y_{lm}(\hat{r}) Y_{lm}(\hat{q}). \qquad (5.13)$$

Planewave matrix elements can be separated into three different contributions: matrix elements between a core and a conduction state, between two core states, and between two conduction states. Since conduction states are expressed in a basis set whereas the core states are solutions of the radial Dirac equation on a grid, the three contributions are to be calculated separately.

5.3.1 Matrix Elements between Two Conduction States

The implementation of planewave matrix elements between two conduction states is described in detail in Refs. [58] and [65], hence the implementation is only sketched here. Using the basis expansion of the conduction state $\psi_{i\mathbf{k}}$ in Eq. (4.9) the planewave matrix element $M_{mn\mathbf{k}}$ is expressed as

$$M_{mn\mathbf{k}}(\mathbf{q} + \mathbf{G}) = \sum_{\mathbf{G'G''}} \left[c_{m\mathbf{G'}}^{\mathbf{k}} \right]^* c_{n\mathbf{G''}}^{\mathbf{k+q}} m_{\mathbf{G'G''k}}(\mathbf{q} + \mathbf{G}), \qquad (5.14)$$

where $m_{\mathbf{G'G''k}}(\mathbf{q} + \mathbf{G})$ is the planewave matrix element between two basis functions $\phi_{\mathbf{G'+k}}$ and $\phi_{\mathbf{G''+k+q}}$:

$$m_{\mathbf{G'G''k}}(\mathbf{q} + \mathbf{G}) = N_k \int d^3r \phi_{\mathbf{G'+k}}^*(\mathbf{r}) \exp(-i(\mathbf{q} + \mathbf{G})\mathbf{r}) \phi_{\mathbf{G''+k+q}}(\mathbf{r}). \qquad (5.15)$$

In the LAPW+LO basis, the integral is separated into contributions from the MT spheres and from the interstitial region. Since the basis contains LAPW functions as well as local orbitals, four different integrals have to be calculated within the muffin-tin spheres: matrix elements between two LAPW basis functions, a local orbital and a basis function, a basis function and a local orbital, and two local orbitals. This yields a total of five different integrals, of which only the integral in the interstitial region can be evaluated analytically.

5.3.2 Matrix Elements between Core and Conduction States

Planewave matrix elements between a core state μ and a conduction state m are denoted by $M_{\mu m\mathbf{k}}$. In order to calculate the matrix elements between the atom-centered functions, the center of integration is shifted to the nuclear position $\mathbf{R}_\alpha$ by inserting $\mathbf{r} = \mathbf{R}_\alpha + \mathbf{r'}$:

$$M_{\mu m\mathbf{k}} = \int_{\Omega_0} d^3r \psi_\mu^*(\mathbf{r}) \mathrm{e}^{-i(\mathbf{q}+\mathbf{G})\mathbf{r}} \psi_{m\mathbf{k}}(\mathbf{r}) = \int_{\Omega_0} d^3r' \psi_\mu^*(\mathbf{r'}) \mathrm{e}^{-i(\mathbf{q}+\mathbf{G})(\mathbf{R}_\alpha+\mathbf{r'})} \psi_{m\mathbf{k}}(\mathbf{r'}) \quad (5.16)$$

$$= e^{-i(\mathbf{q}+\mathbf{G})\mathbf{R}_\alpha} \int_{\Omega_0} d^3r' \psi_\mu^*(\mathbf{r}') e^{-i(\mathbf{q}+\mathbf{G})\mathbf{r}'} \psi_{m\mathbf{k}}(\mathbf{r}').$$

Thus, the integral is reduced to an integration in one muffin-tin sphere with an atom-specific structure factor defined as $S(\mathbf{q}+\mathbf{G}) = e^{i(\mathbf{q}+\mathbf{G})\mathbf{R}_\alpha}$. Using the expansion of planewaves shown in Eq. (5.13), the matrix element are now expressed as the product of radial and spherical contribution:

$$M_{\mu m\mathbf{k}}(\mathbf{q}+\mathbf{G}) = 4\pi S^\star(\mathbf{q}+\mathbf{G}) \sum_{ll'} \sum_{mm'} R_{\mu m(\mathbf{k}+\mathbf{q})}^{ll'm'}(\mathbf{q}+\mathbf{G}) \chi_\mu^{lml'm'}(\mathbf{q}+\mathbf{G}), \qquad (5.17)$$

with the radial contribution

$$R_{\mu m(\mathbf{k}+\mathbf{q})}^{ll'm'}(\mathbf{q}+\mathbf{G}) = \int_{R_{MT}} dr \left(r^2 u^\mu(r) j_l(|\mathbf{q}+\mathbf{G}|r) u_{l'm'}^{m(\mathbf{k}+\mathbf{q})}(r) \right), \qquad (5.18)$$

and the spherical contribution

$$\chi_\mu^{lml'm'}(\mathbf{q}+\mathbf{G}) = C_{lm,l'm'}^\mu Y_{lm}^\star(\mathbf{q}\,\hat{+}\,\mathbf{G}). \qquad (5.19)$$

5.3.3 Matrix Elements between Two Core States

Analogously to the the matrix elements between a core state and a conduction state, the center of integration for matrix elements between two core states is shifted to the atomic position. This introduces the structure factor $S^\star(\mathbf{q}+\mathbf{G})$. The integration is then separated into radial and spherical contribution. The matrix element between two core states can be written as

$$M_{\mu,\mu'}(\mathbf{q}+\mathbf{G}) = 4\pi S^\star(\mathbf{q}+\mathbf{G}) \sum_l R_{\mu,\mu'}^l(\mathbf{q}+\mathbf{G}) \sum_m \chi_{\mu,\mu'}^{lm}(\mathbf{q}+\mathbf{G}) \qquad (5.20)$$

with the radial contribution

$$R_{\mu,\mu'}^l(\mathbf{q}+\mathbf{G}) = \int_{R_{MT}} dr \left(r^2 u^\mu(r) j_l(|\mathbf{q}+\mathbf{G}|r) u^{\mu'}(r) \right), \qquad (5.21)$$

and the sperical contribution

$$\chi_{\mu,\mu'}^{lm}(\mathbf{q}+\mathbf{G}) = C_{lm\mu''}^{\mu'} Y_{lm}^\star(\mathbf{q}\,\hat{+}\,\mathbf{G}). \qquad (5.22)$$

6. Application to TiO$_2$

Core excitations from the $3d$ states in transition metals are particularly hard to capture, due to the spin-orbit coupling between the initial states and strong excitonic effects. Thus, several approaches beyond the independent-particle approximation have been employed to determine the spectra [82][77][39][28][47]. To demonstrate the approach on a well-known example of this material class, it is applied to the the titanium $L_{2,3}$ edge x-ray absoprtion spectrum for rutile TiO$_2$. TiO$_2$ is a semiconducting material, which combines long-term stability, non-toxicity and low-cost availability and has thus attracted substantial interest, both from an experimental and theoretical viewpoint, in the last decades. Its most prominent application is in dye-sensitized solar cells, where TiO$_2$ is used as an electron-transporting substrate [4][24].

In the following, the electronic structure of TiO$_2$ is shortly discussed. For a more detailed treatment, the interested reader is directed to Refs. [73], [38], and references therein. The rutile TiO$_2$ phase is composed of a simple tetragonal structure with experimental lattice parameters of $a = 4.593$ Å and $c = 2.959$ Å.

The unit cell contains two titanium and four oxygen atoms, where the two titanium atoms are equivalent and the oxygen forms two identical pairs. The crystal structure is displayed in Fig. (6.1). Calculations were performed with a **k**-grid of $6 \times 6 \times 9$ and a planewave cutoff of $R_{MT}G_{max} = 7.0$. The convergence of these parameters was determined in Ref. [73]. The left panel of Fig. (6.2) shows the density of states in the unoccupied region. Displayed are the total density of states (TDOS) and the projected density of states of the Ti d- and O p-states. The onset of the conduction band is formed by the Ti d-states, which are hybridized with O p-states. The two distinct bands between 1 eV and 6 eV above the Fermi energy are produced by the crystal-field splitting of the Ti d-states [37]. It is noted, that there is virtually no contribution of Ti d-states to the DOS beyond approximately 6.5 eV.

Figure 6.1: *Unit cell of the rutile phase of TiO$_2$. Titanium atoms are displayed in blue, oxygen atoms in red.*

The $L_{2,3}$ edge absorption spectra are calculated for the titanium atom at the origin of the unit cell. Because of the equivalence of the Ti atoms, the spectra of the second Ti atom in the unit cell is identical[1]. Spectra are found to be converged with a planewave cutoff $R_{MT}G_{max} = 9.0$, a **k**-grid of $4 \times 4 \times 6$, an inlusion of local field effects of $|\mathbf{G} + \mathbf{q}|_{max} = 5\ a_0^{-1}$, 100 empty states for the RPA screening, and 50 unoccupied states in the BSE Hamiltonian.

In order to compare to the experimental spectrum, the anisotropy of the dielectric tensor has to be taken into account. Because of the tetragonal structure, $\epsilon_{M,xx}$ and $\epsilon_{M,yy}$ are equivalent, whereas the ϵ_{zz}-component shows different spectral features. Since no information of the setup of the x-ray absorption measurement was available, an average over the components of the dielectric tensor was applied to compare to the experiment. For the final calculations, a broadening of 150 meV is used. Experimental and calculated spec-
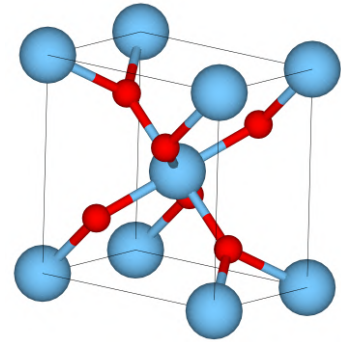
---

[1]The numerical equivalence was tested for several parameter sets and spectra were found to be identical in all caseslowest.
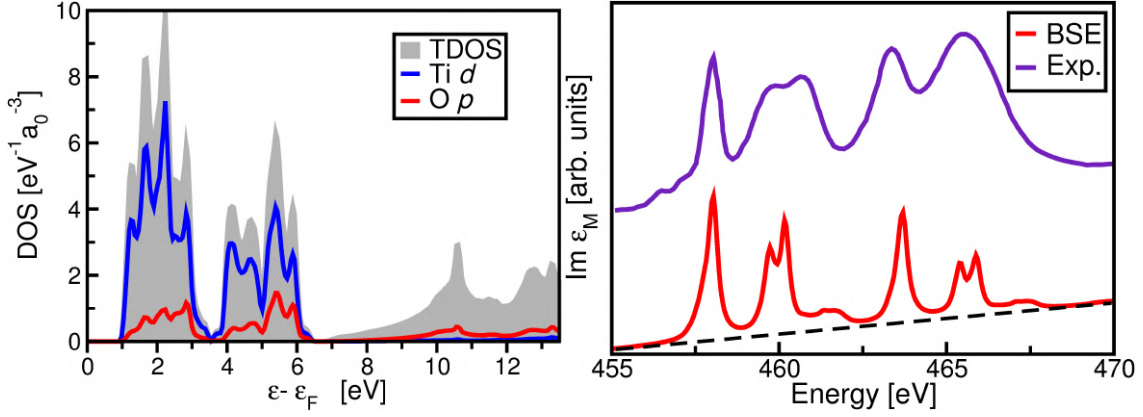
27

Figure 6.2: Left: TiO_2 TDOS, Ti d-state projected DOS, and O p-state projected DOS. For the projected DOS, the different atomic contributions are added. Right: Full spectrum of titanium L_{23}-edge compared to experimental absorption spectrum obtained from [35]. Experimental and calculated spectra are aligned at the first absorption peak.

tra are aligned at the first absorption peak, the calculated spectra are therefor shifted by $\Delta\epsilon = 22.385$ eV.

The comparison between experimental and calculated spectra is shown in the right panel of Fig. (6.2). The experimental spectrum obtained from Ref. [35] shows a distinct linear background, which is not found in our calculations, where the absorption vanishes when the transitions into the Ti d-states are exhausted. For a better comparison between experimental and theoretical spectrum, the linear background is added to the normalized calculated result. The calculated dielectric functions displays the main features of the experimental spectrum: a distinct excitonic peak at 358 eV, followed by a double peak at approximately 460 eV. These features reappear at 464 and 466 eV, respectively. In both spectra, the first peak at 460 eV is less intense than the second one. Compared to experiment, the splitting of the double peak around 360 eV is slightly underestimated. In the experimental spectra, there is also no fine splitting of the broad peak at 466 eV, but previous calculations within the BSE approach [39] and the multichannel approach [36] produced similar fine-structure features. Overall, the agreement with the experimental spectrum is very good, as well as the agreement with previous calculations in the BSE approach [39][68].

The BSE approach allows for the analysis of different contributions to the specra by setting the corresponding terms in the Hamiltonian in Eq. (4.20) to zero. The left panel of Fig. (6.3) shows the resulting spectra. Compared to the independent-particle (IP) calculations, spectra within the full BSE approach are red-shifted to lower energies due to the attractive screened Coulomb interaction. It also introducces the sharp excitonic peaks, which arise from the mixing of independent-particle transitions and represent bound states of the electron-hole exciton.

If the exchange term in BSE Hamiltonian is neglected ($H^x = 0$), the spectra are further red-shifted, since the exchange term is repulsive. Furthermore the excitonic peaks are preserved, since these arise from the direct term in the Hamiltonian. One also sees that without the exchange interaction the branching ratio is shifting towards the statistical value of $2 : 1$, since intensity is shifted from the L_2 peaks back to the L_3 ones. The influence of the exchange term on the branching ratio in the $L_{2,3}$ XAS of TiO_2 was
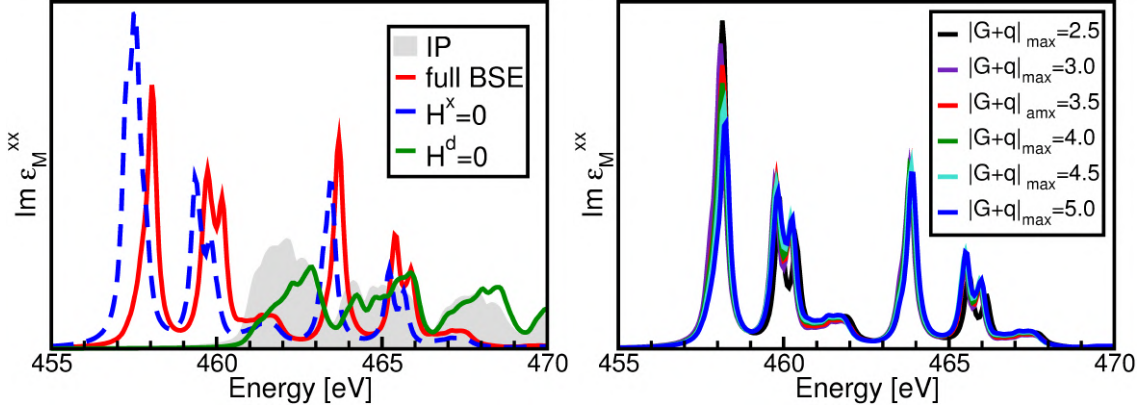
Figure 6.3: Left: Influence of the different contributions to the BSE Hamiltonian. Displayed are the spectrum in the independent-particle (IP) approximation in shaded grey, with the full Hamiltonian (BSE) in the solid red line, with the exchange term set to zero ($H^x = 0$) in the dashed blue line and with the direct term set to zero ($H^d = 0$) in the solid green line. Right: TiO_2 titanium $L_{2,3}$ for different values of $|\mathbf{G} + \mathbf{q}|_{max}$.

already observed by Ref. [39], where it is shown that exchange terms are necessary to reproduce the experimental branching ratio. The importance of local field effects in the exchange interaction for core excitations was also discussed in Ref. [62]. If the direct term is neglected ($H^d = 0$), the spectrum resembles the IP one, since without the attractive potential neither excitonic peaks, nor the overall red-shift occur. On the contrary, the repulsive exchange term blue-shifts the spectrum.

The influence of local field effects can now be determined in more detail. By obtaining spectra for different values of $|\mathbf{G} + \mathbf{q}|_{max}$, the dependence of the spectra on the local field effects is determined. The results are shown in the right panel of Fig. (6.3). With an increasing value of $|\mathbf{G}+\mathbf{q}|_{max}$, the oscillator strength of the first absoprtion peak at around 435.7 eV is reduced, whereas the intensity of the second and fourth peak are increased. Overall, the relative intensity between the first and the other peaks is reduced. Thus, the local field redistributes from the first peak to the second and fourth. The first absorption peak is also found to be slightly blue shifted with an increased value for $|\mathbf{G} + \mathbf{q}|_{max}$, as the repulsive exchange interaction is increased.

Our approach allows us to analyze separately the contribution of different intial core states to the spectrum. The left panel of Fig. (6.4) displays the imaginary part of the xx-component of the dielectric tensor. L_2 denotes contributions from the $2p_{1/2}$-states alone, L_3 transitions from the $2p_{3/2}$, and *cross terms* denote differences between the total L_{23} spectrum and the sum of the L_2- and L_3-transitions. One sees that, as expected, the first two peaks at lower energies are due to L_3-transitions, whereas the two peaks at higher energies are due to L_2-transitions. The cross terms between the transitions shift intensity from the L_3- to the L_2-transitions, thereby reducing the so called *branching ratio*, which describes the relative intensity of the L_3 spectrum compared to the L_2 spectrum. In the independent particle picture, the branching ratio is given by the ratio between the number of M_J-states, such that the branching ratio for L_{23}-spectra is $2 : 1$. It has alrady been reported [39], that the mixing of $2p_{1/2}$ and $2p_{3/2}$ states due to the electron-hole interaction has to be included to explain the branching ratio of approximately 1:1 in rutile TiO_2. Since the cross-terms reduce the intensity in the L_3-branch and shift it to the L_2 branch,
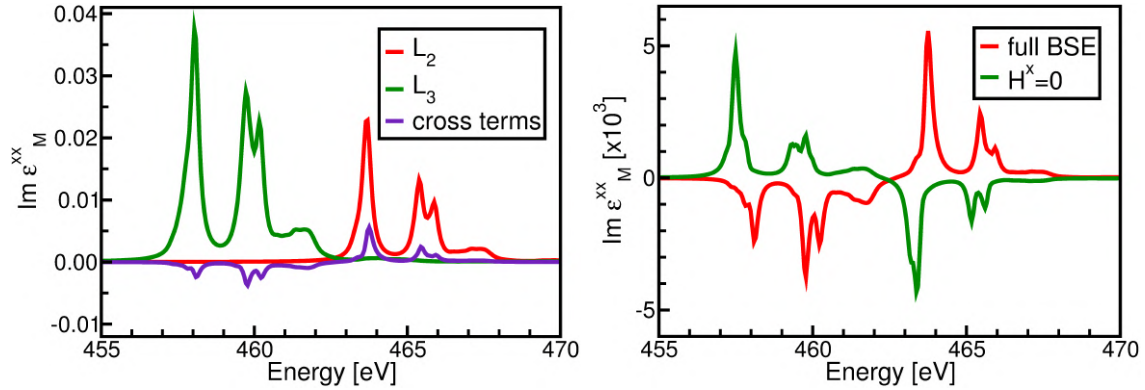
Figure 6.4: Left: Sepa+ration of the Ti $L_{2,3}$ absorption spectrum in L_2-, L_3-, and cross-term contributions. Right: Cross terms as obtained from a full BSE calculations (red) and a calculation where the exchange terms is omitted ($H^x = 0$, blue).

the branching ratio is reduced. To determine whether the inclusion of local field effects affects mainly the exchange interaction, as was argued in Refs. [39] and [62], the cross terms was calculated using the full BSE Hamiltonian and without the exchange term separately. The results are shown in the right panel of Fig. (6.4). Cross terms occur in both calculations in the same order of magnitude, but with opposite sign: While in a full BSE calculation intensity is shifted from the L_3- to the L_2-transitions, in a calculation without the exchange interaction intensity shifts from the L_2- to the L_3-transitions. This indicates that local field effects influences both direct and exchange interaction. While in the direct term, local field effects induce a greater attractive term, thereby shifting intensity to lower energies, the opposite occurs in the exchange interaction. Local field effects increase the repulsive exchange interaction, thus shifting intensity to higher energies. In the full BSE Hamiltonian, both of the competing effects occur, indicating that the influence is bigger on the exchange term than on the direct term.

In summary, the influence of mixed transitions from $2p_{1/2}$ and $2p_{3/2}$ on the Ti $L_{2,3}$ absorption spectrum of rutile TiO_2 is observed. It is shown that for this edge, excitonic effects and spin-orbit effects have to be taken into account to reproduce the spectra. The deviation of the branching ration away from the statistical value can only be explained if the short-range exchange effects are treated carefully. The implementation presented here allows a detailed analysis of the influence of local field effects, which indicate that not only the exchange but also the direct interaction is crucially influenced by them. In good agreement with previous calculations [62], local field effects are observed to be crucial in the description for spectra, for which the independent-particle picture fails.

Part II

X-Ray Absorption Spectroscopy of MAPbI$_3$

7. Introduction

Hybrid organic-inorganic halide perovskites have emerged in the last few years as photovoltaic materials with tremendous success. Starting from the seminal work in 2009 [34], solar cells based on these materials have reached a power convergence efficiency (PEC) of close to that of silicon-based cells [40][44][79]. New record PEC values are published at an unprecedented speed, leading to perovskite solar cell being the *"next big thing in photovoltaics"* [8]. These dye-sensitized solar cells consist of a substrate of mesoscopic TiO_2, on which a layer of the hybrid organic-inorganic perovskite is deposited. The active layer is topped by a solid hole transporting material. This development has sparked great interest in the structural, electronic and optical properties of the hybrid organic-inorganic halide perovskites. Despite the success of the materials in photovoltaics, little was known about the underlying material properties. Due to the application in photovoltaics, electronic and optical properties have been the focus of the *ab initio* investigations. The electronic structure has been studied using DFT [49][10][45], and state-of-the-art *GW* methods [11][74][17] focusing on the determination of the fundamental band gap. Optical properties of $CH_3NH_3PbI_3$ have been studied using the BSE approach [1].

Compared to the effort invested in the determination of the electronic structure and the optical properties, little is known about the core excitations of the materials, which yield information on the unoccupied states beyond the band gap and can therefore provide further indications on the electronic properties in the near-gap region. Here, the first *ab initio* study of the x-ray absorption near-edge spectra (XANES) for $CH_3NH_3PbI_3$ is presented.

Perovskite denotes the crystal structure of the mineral $CaTiO_3$, which is adopted by a large family of materials with the formula unit ABX_3. The most notable example of these are $SrTiO_3$ and $BaTiO_3$. The inorganic perovskites are known for their structural complexity [12], with many different phases observed. Perovskites have been found with cubic, tetragonal, orthorhombic, trigonal, and monoclinic phases [21]. The hybrid organic-inorganic perovskites are produced by a molecular cation, most commonly $CH_3NH_3^+$ or NH_4^+, at the position A, a metal cation, such as Pb^{2+} or Sn^{2+} in the B position, and a halide anion, typically I^- or Br^- in the X position. The prototypical material of this class, $CH_3NH_3PbI_3$ is studied in this work. The structure consists of a network of PbI_6^- octohedra, with the Pb^{2+} in the center and the I^- on the corners. The cavities between the octohedra are filled

Figure 7.1: *Crystal structure of the high-temperature cubic phase of $CH_3NH_3PbI_3$*

with the $CH_3NH_3^+$ molecules (see Fig. (7.1)). Due to the possible tilting of the octohedra, the characterization of the crystal structure for perovskite materials is a challenging task, especially so for the organic-inorganic hybrid perovskites. The structural properties have been investigated using DFT [12][5] and molecular dynamics [60]. Three phases of $Ch_3NH_3PbI_3$ have been identified [72][6]: a low-temperature tetragonal ($I4/mcm$) phase, an intermediate orthorhombic ($Pnam$) phase at room temperature and a high-temperature
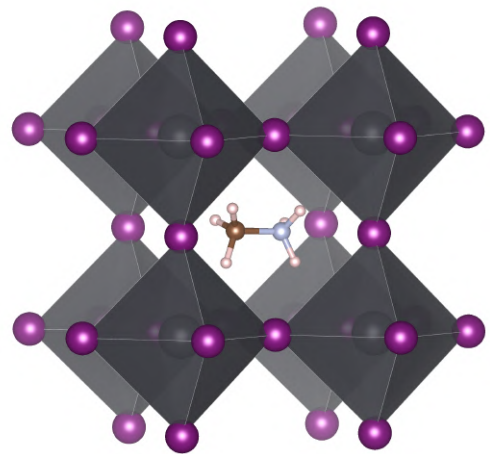
pseudocubic phase ($Pm\bar{3}m$). In this work, focus lies on the high-temperature phase, since its unit cell contains only one chemical unit, thus allowing for the application of the computationally expensive BSE approach. Experimental lattice parameter $a = 6.3115$Å and atomic positions from [72] were used, furthermore the pseudocubic lattice was replaced by a full cubic one. Since the deviation from the cubic lattice parameters is very small, this results in a change of the unit cell volume of only 0.08%. Since the position of the hydrogen atoms cannot be resolved in x-ray-based crystallographic methods [46], these atoms were added at molecular positions around the C and N atom, and the organic group was relaxed. It has been shown that the orientation of the organic group has only minor influence on the bandstructure in the cubic phase [13], therefore the influence of different molecular orientations is not investigated in this work.

In order to determine the influence of organic states on the electronic structure, especially the hybridization between Pb and I states and the molecular states, the spectra of $CH_3NH_3PbI_2$ are compared with those of PbI_2. PbI_2 is a layered semiconducting material, which is the binary compound from which $CH_3NH_3PbI_3$ is produced. Within its hexagonal crystal phase (space group $P\bar{3}m1$, number 164) [78], PbI_2 forms a layered structure, where the two planes containing iodide atoms lie between the planes formed by lead atoms. Structure optimization yields the lattice parameters $a = 4.54$Å and $c = 6.98$Å in good agreement with experiment.

Here the following notation is introduced: $MAPbI_3$ will be used as a shorthand notation, where MA stands for the methyl ammonium molecule, instead of refering to the full name of the hybrid organic-inorganig hybrid halide perovskite as $CH_3NH_3PbI_3$.

8. Electronic Structure

The x-ray absorption strongly depends of the local electronic structure at the absorbing atom. Therefore the electronic structure of the organic-inorganic hybrid perovskite $MAPbI_3$ is evaluated in the following chapter in comparison to the binary compound PbI_2. Convergence of the total energy yields a parameter set of $R_{MT}|\mathbf{G} + \mathbf{k}|_{max} = 4.7$, a $\mathbf{k}$-grid of $4 \times 4 \times 4$ for $MAPbI_3$ and $R_{MT}G_{max} = 10$ and a $\mathbf{k}$-grid of $6 \times 6 \times 4$ for PbI_2. All electronic structure calculations were performed with the PBEsol GGA functional [57].

In the hybrid perovskite $MAPbI_3$, the presence of the organic group can significantly influence the electronic structure through hybridization effects. Since focus lies on core transitions in the inorganic atoms, only the hybridization of lead and iodide states with these *organic* states is considered, without specifying to which atom and l-channel of the organic group these states belong.

As shown in Fig. (8.1), the low-energy region of the DOS, up to 2.6 eV above the Fermi energy, has mainly Pb p character, which exhibits hybridization with I p-states. The first peak in the DOS at 1.4 eV is dominated by contributions from the Pb p-states, whereas the second peak at 2.8 eV has nearly equal contributions from Pb and I p-states. There are also small contributions from d-states and organic states to the second peak. In the second region from 3.5 to 8.4 eV, the DOS has mainly I p character, with significant contributions from Pb p-states as well as from organic states. The contributions from organic states are clearly visible in Fig. 8.2. At even higher energies beyond 8.5 eV, the DOS has mainly I d character, with significant contributions from I f-states at energies higher then approximately 10 eV (see left panel of Fig. 8.2).

The band structure of the hybrid organic-inorganic perovskite $MAPbI_3$ is displayed in Fig. (8.1). The Kohn-Sham eigenvalues are displayed along the $Pm\bar{3}m$ symmetry line $\Gamma - R - X - M - \Gamma - X$, although the inversion symmetry is broken due to the presence of the organic group in the center of the unit cell. This approach has already been employed by Gao *et al* [19]. The band structure up to 10 eV beyond the band gap is shown in Fig. (8.3) together with the partial density of states of the significant inorganic states. The low energy bands below approximately 2.6 eV are highly dispersive, as stated above these bands are predominately formed by the lead p-states. The minimum of the conduction band is found at the R point. At higher energies, much less dispersive bands occur. Here, the hybridization with the less dispersive molecular states is visible.

Our results are in agreement with previous calculations of the electronic structure of $MAPbI_3$ in the high temperature phase [75][80][54]. Calculations performed with a linear combination of atomic orbitals [75] obtained iodide $5p$ and lead $6p$ states in the valence region of approximately 5 eV beyond the band gap. But since that work replaced the organic group CH_3NH_3 by a uniform background charge density, hybridizations with organic states were ignored. More recent calculations [54][80], which explicitly take the organic group into account, also obtained the mainly lead p-state character of the lowest conduction states and the high hybridization of iodide s-, p- and d-states at the onset of the conduction band. Since in that work only the character of the lowest unoccupied bands was of interest, the density of states was only calculated up to 2 eV above the band gap. The obtained band structure is in good agreement with previous results at the same level of theory [19]. For the core states, a spin-orbit splitting of 298.611 eV between the iodide $2p_{1/2}$ and $2p_{3/2}$ states and a splitting of 103.97 eV between the lead $3d_{3/2}$ and $3d_{5/2}$ states
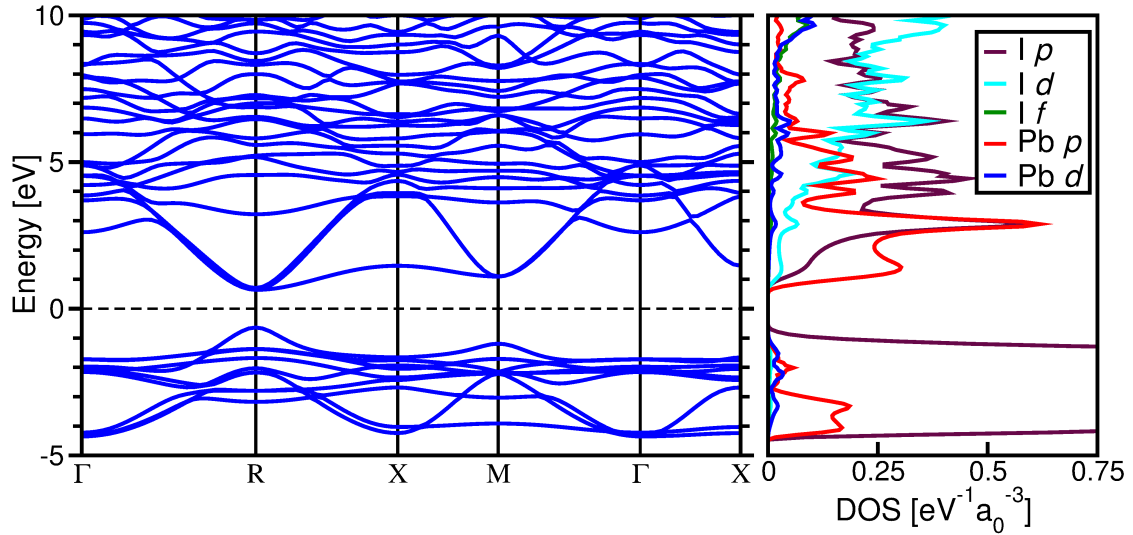
Figure 8.1: Band structure of MAPBI$_3$ and projected density of states for the low-energy region around the band gap. The energies are relative to the Fermi energy.
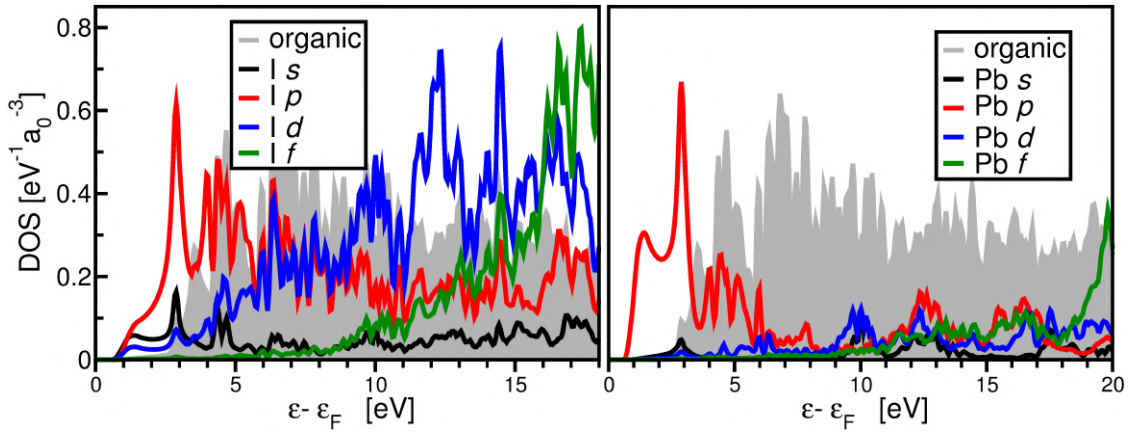

Figure 8.2: Projected density of states for the iodide (left) and lead atoms (right) in MAPbI$_3$. The grey area displays the total density of states of the organic group.

is obtained.

The electronic structure of MAPbI$_3$ is now compared with that of the binary compound PbI$_2$. Due to the different crystal structure, the density of states is compared instead of the full band structures. As in the case of MAPbI$_3$, focus lies mainly on the unoccupied region of the band structure, which is probed in the x-ray spectroscopy.

Figure (8.3) shows the projected unoccupied DOS for the iodide and lead atoms in PbI$_2$. The DOS has a distinct peak at the onset of the bandgap (between 1.2 and 3.5 eV above the Fermi energy). This strong peak has mainly Pb p character. While other Pb states do not contribute to the DOS in this energy region, strong contributions from I p-states occur. These I p-states are also hybridized with I s- and d-states in this energy region. At energies above 3.5 eV, contributions from Pb states are small, the DOS is dominated by iodide states. Between 3.5 and 12 eV, the contributions are mainly from I $p-d$ hybridized states, between 12 and 16 eV from I $d-f$ hybridized states. At higher energies dominant contributions arise from the I f-states.
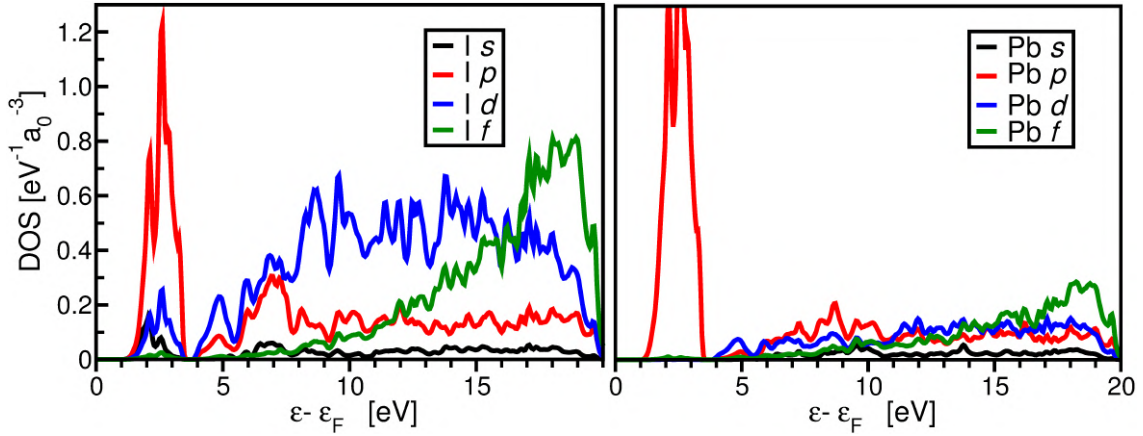
Figure 8.3: Projected density of states for the iodide (left) and lead (right) atoms in PbI_2. The energies are denoted relative to the Fermi energy and only the spectrum of unoccupied states is displayed.

In summary a sharp unoccupied band of lead p-states hybridized with iodide p-states is observed above the band gap. The band extends over approximately 2.3 eV. A broader band of mainly I d-states extends over a large energy region beyond 3.5 eV, these states are mostly localized to the iodide atoms although there is some hybridization with the lead d-states.

For the core states, calculations yield a spin-orbit splitting of 298.51 eV between the iodine $2p_{1/2}$ and $2p_{3/2}$ as well as a splitting of 103.94 eV between the lead $3d_{3/2}$ and $3d_{5/2}$ states.

9. Iodide $L_{2,3}$ Absorption Spectra

The determination of core-level spectra starts with an investigation of the spectra of I $L_{2,3}$ edge transitions for MAPbI$_3$ and the binary compound PbI$_2$. Due to the large spin-orbit splitting of 298.61 eV between the iodide $2p_{1/2}$ and $2p_{3/2}$ states in MAPbI$_3$, transitions from the I $2p_{1/2}$ and $2p_{3/2}$ states are decoupled and the resulting spectra can be calculated separately, taking only the corresponding states of the subedge in the BSE Hamiltonian into account.

Convergence test were performed for the main parameters of the BSE calculations. These are the number of **k**-points, the planewave cut off $R_{MT}G_{max}$, the number of unoccupied states in the RPA screening, the number of unoccupied states in the BSE Hamiltonian and the cut off for local field effects $|\mathbf{G} + \mathbf{q}|_{max}$. A k-grid of $4 \times 4 \times 4$, $R_{MT}G_{max} = 4.7$, 100 unoccupied states in the RPA-screening, and $|\mathbf{G} + \mathbf{q}|_{max} = 2.0\,a_0^{-1}$ yield a converged spectrum.

Figure (9.1) shows the imaginary part of the xx-component of the macroscopic dielectric tensor. It can be seen, that the spectral features of the iodide L_2- and L_3-edge absorption are identical, the relative intensity between the two subedges is caused by the different number of initial states. While the L_3 absorption includes transitions from the 4 $2p_{3/2}$ states, the L_2 absorption contains only transitions from the 2 $2p_{1/2}$ states. The inclusion of electron-hole interaction shifts the absorption to lower energy compared to calculation in the independent-particle (IP) approximation due to the attractive Coulomb interaction between electron and hole. While oscillator strength is shifted to low-energy peaks, the main peaks are already visible in the independent-particle spectrum. Figure (9.3a) displays the oscillator strength of the excitons in the full BSE calculation and the IP calculation without broadening for the L_2 edge. In the IP picture, a band of excitons between 4770 eV and 4771 eV with similar oscillator strength is followed by a small gap of roughly 0.5 eV in which only three excitons with very weak oscillator strength occur. Beyond this gap, a broad band of excitons extends towards 4790 eV. Since in the IP approximation, the spectrum is proportional to the unoccupied projected density of states weighted by the momentum matrix elements between the core and the unoccupied states, the IP spectra can be compared with the DOS already shown in the left panel of Fig. (8.2) and the in Fig. (8.3). The first group of excitons corresponds to the iodide p-states at the onset of the conduction band, which are hybridized with the iodide s-states. The spectral features in the extended band starting at 4771 eV can be mapped to the iodide d-states beyond 7 eV above the Fermi energy. This behavior is expected since the selection rules favor transitions to the iodide s- and d-states. Since the unoccupied DOS of the s-states is much smaller than the one of the d-states, transitions into d-states dominate the spectrum.

In the BSE calculations, oscillator strength is shifted towards lower energies as stated above. While in the IP spectrum excitations have comparable oscillator strength over large energy intervals, in the full BSE a few single excitons with strong relative oscillator strength are observed. One can see that the transitions in the energy region between 4772 and 4776 eV are favored in the BSE, as the oscillator strength of excitons in this region is higher in the BSE than in the IP calculations. Thus, the absorption of the low-energy part of the extended iodide p-band is more intense in the BSE calculations. In the same way, transitions around the band gap edge at 4770 eV occur. Figure (9.3a) displays the oscillator strength of the excitons contributing to the xx- component of the dielectric
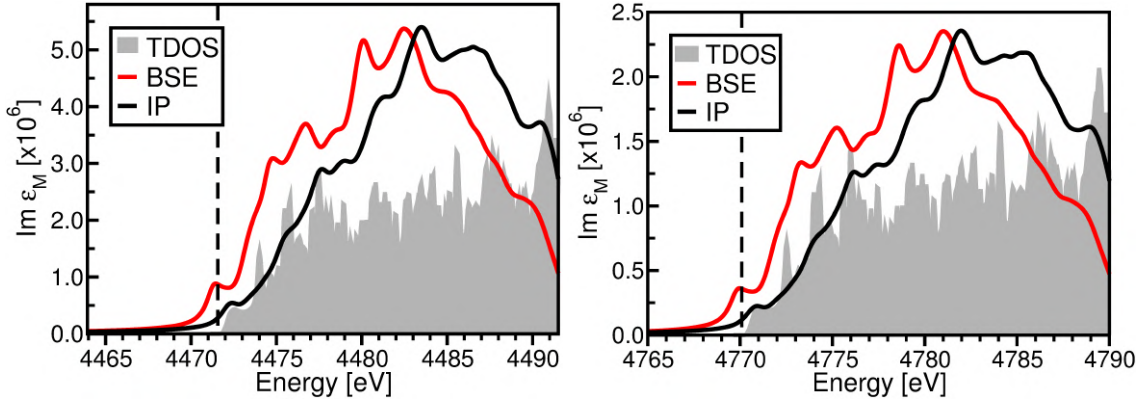
Figure 9.1: Iodide L_3 (left) and iodide L_2 (right) absorption spectrum for MAPbI$_3$. The total density of states (TDOS) is shown in grey, the dotted line denotes the absorption onset in the independent particle (IP) approximation.

tensor. A weakly bound exciton is formed with intense oscillator strength at 4769.89 eV, which dominates the first peak in the BSE spectrum. The binding energy of this exciton is 479 meV. Another group of excitons can be seen in the low-energy region of the extended iodide d-band. The excitons with biggest oscillator strength occur at approximately 4772 eV, and the oscillator strength is decreasing with increasing energy. This is different from the IP spectrum, where the oscillator strength increases with increasing energy at the onset of the band. Local-field effects have no significant influence on the spectrum (compare Appendix A). This indicates that the difference between the IP and BSE spectrum is due to the screened core hole, and that many-body effects are weak in this spectrum.

The atomic contributions of the three iodide atoms in the unit cell are added to obtain the total absorption. The molecular axis of the organic CH$_3$NH$_3$-group breaks the crystal symmetry of the simple cubic lattice spanned by the inorganic frame. Therefor an anisotropy in the dielectric tensor is observed, i.e. a normal and a parallel component. In order to analyze the contributions to the dielectric tensor in more detail, the different iodide atoms in the unit cell are considered[see Fig. (9.2)]. Due to their symmetric orientation with respect to the organic group, the iodide atoms I1 and I2 in the xy-plane of the unit cell contribute symmetrically to the dielectric tensor, i.e. $\epsilon_{M,xx}(\text{I1}) = \epsilon_{M,yy}(\text{I2})$,

Figure 9.2: Unit cell of pseudocubic MAPbI$_3$. I1, I2, and I3 denote the different iodide atoms in the unit cell.

$\epsilon_{M,yy}(\text{I1}) = \epsilon_{M,xx}(\text{I2})$ and $\epsilon_{M,zz}(\text{I1}) = \epsilon_{M,zz}(\text{I2})$. The contributions from the atom I3 are different from the contributions from atom I1 and I2, but due to the symmetry $\epsilon_{M,xx}(\text{I3}) = \epsilon_{M,yy}(\text{I3})$. This yields for the total dielectric tensor, that $\epsilon_{M,xx} = \epsilon_{M,yy}$ is the contribution normal to the molecular axis and $\epsilon_{M,zz}$ is the contribution parallel to the molecular axis. This requires a detailed analysis of the five distinct atomic contributions and the two different total components. Figure (9.3b) shows the different atomic contributions to the xx-component of the dielectric tensor for the L_2 edge. While the spectra of the different atoms show some difference in oscillator strength, the position of the peaks
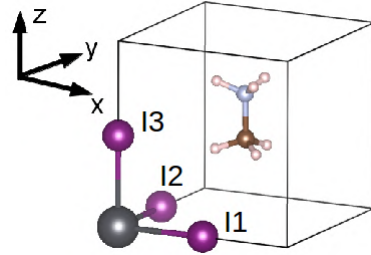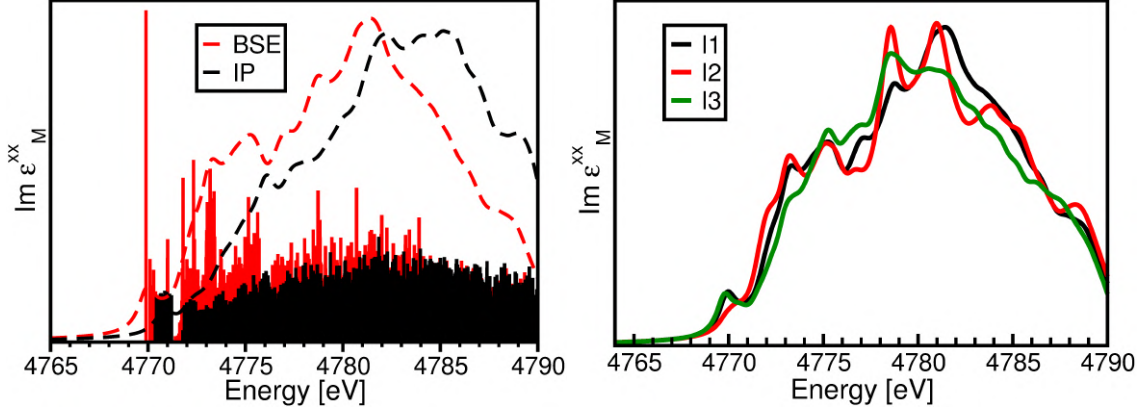
Figure 9.3: Left: Excitation energies (vertical bars) and their oscillator strength indicated by the height of the bars for a BSE calculation (red) and a calculation in the IP approximation (black). The corresponding spectra are shown for reference. Right: Atomic contributions to the iodide L_2 spectrum. For the positions I1, I2 and I3, see Fig. (9.2).
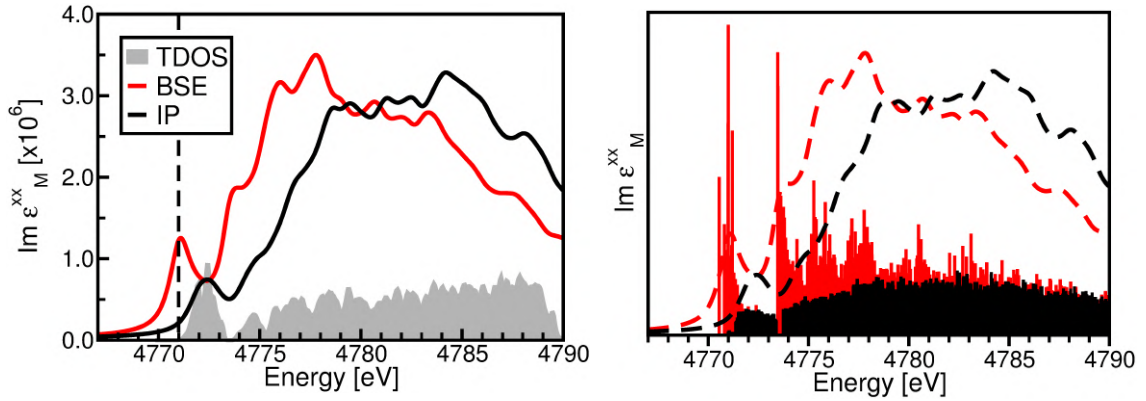

Figure 9.4: Iodide L_2 spectrum of PbI_2 from the solution of the BSE (red) and in the IP approximation (black). For comparison, the total DOS is shown in the left panel, while the right panel indicates the excitation energies (vertical bars) and their oscillator strengths (height of the bars).

is the same. The most notable difference between the components is the relative intensity of the first peak at approximately 4770 eV. This peak is well pronounced in the $\epsilon_{M,xx}(I1)$- and $\epsilon_{M,xx}(I3)$-contribution, but only a weak shoulder in the $\epsilon_{M,xx}(I2)$-contribution. Instead, in this component, oscillator strength is shifted to peaks at higher energies around 4780 eV. The iodide L_2 spectrum of the hybrid perovskite is now compared with that of the binary compound PbI_2. Figure (9.4a) shows the total absorption spectrum of PbI_2, consisting of the two atomic contributions from the iodide atoms in the unit cell. Calculations were performed using a k-grid of $7 \times 7 \times 5$, $R_{MT}G_{max} = 11.5$, 100 empty states in the RPA screening [see Eq. (4.28)], and $|\mathbf{G} + \mathbf{q}|_{max} = 3.0$. The two atoms have been found to have nearly equivalent contributions, due to the equal orientation with respect to the lead atom. The spectra shows similar features compared to the perovskite one: The BSE spectrum displays a peak at the onset of the IP absorption, followed by a broad absorption band. As in the case of the hybrid perovskite, the inclusion of many-body

effects red-shifts the spectrum while also localizing the oscillator strength in fewer excitations compared to results obtained in the IP approximation [see Fig. (9.4b)]. Different from the perovskite case is the low-energy absorption: Already in the IP spectrum, the first peak at 4772 eV is more pronounced. Comparison with Fig. (8.1a) reveals that this peak represents transitions into the sharp peak of iodide p-states, which is observed in the DOS. Although transitions into p-states are dipole-forbidden, I s- and d-states also contribute to the DOS in this region, offering dipole-allowed transitions. With the inclusion of excitonic effects, the peak is shifted to lower energies and a group of bound excitons occur. The calculations yield ten bound excitons with binding energies of up to 448 meV, whereas only one weakly bound exciton is found in the spectrum of MAPbI$_3$. Interestingly, changes in the $\mathbf{k}$-grid during the convergence tests mainly affect the high-energy behavior, whereas the first peak in the spectrum is well converged with a lower grid (compare Appendix A). This indicates that the first peak represents a delocalized excitation, which is well described with a small sampling of $\mathbf{k}$-points.

10. Pb $M_{4,5}$ Absorption Spectra

The Pb $M_{4,5}$ edge absorption spectrum is calculated for MAPbI$_3$ and the binary compound PbI$_2$. Results obtained from full BSE calculations are compared to results in the independent-particle approximation in order to determine the influence of excitonic effects on the spectra. Convergence with respect to the main parameters of the BSE calculations are performed, one obtains $R_{MT}G_{max} = 4.7$ and $|\mathbf{G} + \mathbf{q}| = 1.0$. Convergence tests yield a $\mathbf{k}$-grid of $6 \times 6 \times 6$ and 100 unoccupied states in the RPA screening. The Pb $M_{4,5}$ edge absorption spectrum for PbI$_2$ is calculated using converged parameters of $|\mathbf{G} + \mathbf{q}|_{max} = 2.0$, a $\mathbf{k}$-grid of $8 \times 8 \times 6$, $R_{MT}G_{max} = 10.0$, and 100 unoccupied states in the RPA screening obtained from convergence studies.

As in the case of iodide $L_{2,3}$ absorption spectra of MAPbI$_3$, the large spin-orbit coupling of the core states- 103.97 eV between the lead $2d_{3/2}$ and $2d_{5/2}$ states- allows for the independent calculation of lead M_4- and M_5-absorption spectra. Due to the higher numbers of initial core states in the M_5-edge, the number of unoccupied states in this edge was limited to 40, whereas in the M_5-edge 50 unoccupied states is used. The binding energies of the low-energy excitons are already converged with less then 40 unoccupied states, since high-energy unoccupied states only contribute to the absorption in the extended band of lead f-states.

The resulting spectra are displayed in Fig. (10.1). The two sub-edges exhibit identical spectral features, but the overall scale of the spectrum is bigger in the M_5 absorption. The difference in relative intensity is due to the different number of initial core states in the transitions: the M_5-spectrum represents transitions from the 6 $3d_{3/2}$ states, the M_4-spectrum from the 4 $3d_{1/2}$ states. The lead M_4 spectrum is discussed in the following.

In the IP approximation, double peaks at 2539 eV and 2541 eV are followed by a region of weaker absorption and a gradual increase in the absorption at around 2546 eV. Interestingly, these features can not be seen TDOS, which shows a pronounced peak at approximately 2540 eV, where the spectrum displays a local minimum. The gradual increase at higher energies can not be seen in the TDOS either. If one compare the spectrum with the partial DOS of Figs. (8.2) and (8.3), it is apparent that the first peak at 2539 eV in the absorption spectrum is due to transitions to the lead p-states, which in this energy-region are mostly hybridized with the iodide p-states. The second peak at 2541 eV is due to iodide p-states that are strongly hybridized with iodide p-states as well as the organic states. The absorption then decreases as the lead p-state DOS decreases and the lead f-state contribution is still weak. The increase of absorption at 2546 eV is then due to the lead f-states that dominate the DOS at high energies.

Employing the full BSE approach distinctively changes the spectrum. A strong peak appears at 2537 eV, below the onset of IP absorption. It is followed by a weak shoulder at 2538.5 eV. A second, much weaker peak can be seen at 2540 eV. A strong increase of the absorption is observed starting from 2545 eV. Compared to the IP spectrum, changes in the high-energy region are minor. The absorption to the lead f-states is red-shifted by approximately 1 eV due to the attractive electron-hole interaction, but the spectral features are unchanged. Figure (10.2a) shows the excitons of the M_4 edge absorption spectrum: The first absorption peak at approximately 25307 eV is formed by three excitons with intense oscillator strength, two of which are located at 25307.03 eV and one at 2537.04 eV. These have binding energies of 863 meV and 738 meV, respectively. Two more group
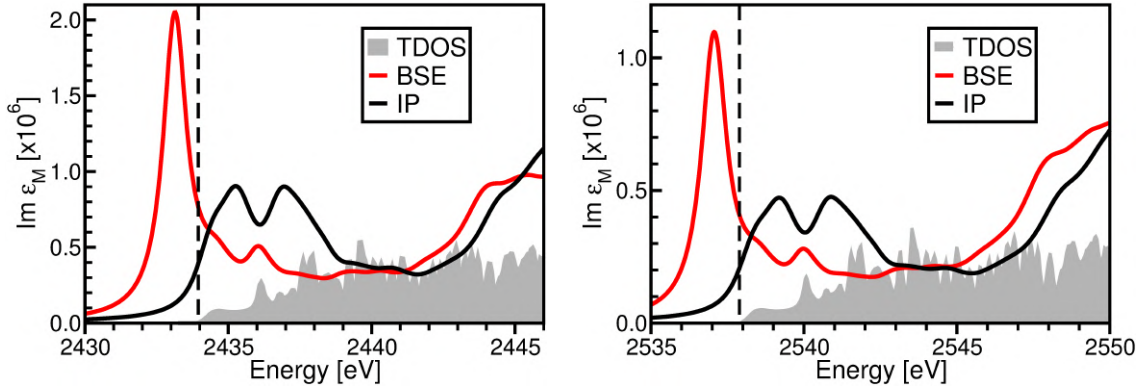
Figure 10.1: Lead M_5 (left) and lead M_4 (right) absorption spectra for $MAPbI_3$ from solutions of the BSE (red) and in the IP approximation (black). The total density of states (TDOS) is shown in grey, the dotted line denotes the absorption onset in the IP approximation.

of excitons are observed at 2538.5 eV and 2540 eV. As in the case of the iodide $L_{2,3}$ edge spectrum, these transitions are red-shifted compared to the IP transitions. One also observe a localization of oscillator strength to a few excitons. The transitions to the extended f-band are also red-shifted in the BSE compared to the IP spectrum, without major localization of the oscillator strength.

Due to the anisotropy of the unit cell, the dielectric tensor has two unique components with different spectral features. The numerical equivalence $\epsilon_M^{xx} = \epsilon_M^{yy}$ is found, representing the component perpendicular to the molecular axis of the CH_3NH_3 group [compare Fig. (9.2)]. The component ϵ_M^{zz} shows different spectral features, as it describes the component parallel to the molecular axis. As displayed in Fig. (10.3b), there are only slight differences compared to the perpendicular component. The main absorption peak occurs in both spectra, but the intensity of the second peak is reduced in the parallel component. The shoulder at 2538.5 eV is not visible in the parallel component, as the cluster of excitonic peaks in this region in the perpendicular component [displayed in Fig. (10.2a)] does not appear in the parallel one.

The Pb $M_{4,5}$ edge absorption spectrum for PbI_2 is shown in Fig. (10.3a). In the IP approximation, a sharp peak is observed at 2539.5 eV followed by a broader peak around 2547 eV. At higher energies, a sharp increase in the absorption is observed. Comparison with the density of states shows that the first peak is produced by transitions into Pb p-states, which dominate the DOS in this energy region [compare Fig. (8.3)]. The absorption beyond the first peak is produced by the hybridized Pb p- and Pb f-states. As in $MAPbI_3$, the inclusion of electron-hole interaction introduces an intense bound excitonic peak below the band gap. The peak is formed mainly by two excitons with high oscillator strength [see left panel of Fig.(10.3)]. The two excitons have binding energies of 953 meV and 896 meV, respectively. The absorption at higher energies is slightly red-shifted by the electron-hole interaction, but the spectral shape is unchanged. Thus, the main influence of the interaction is the formation of tightly bound excitonic states from the Pb d-states. The binding energies of these excitons are slightly higher than in $MAPbI_3$. The second peak, observed in the $MAPbI_3$ spectrum, can not be seen in the PbI_2. This indicates that this peak is formed by transitions into the Pb d-states hybridized with states of the organic compound.
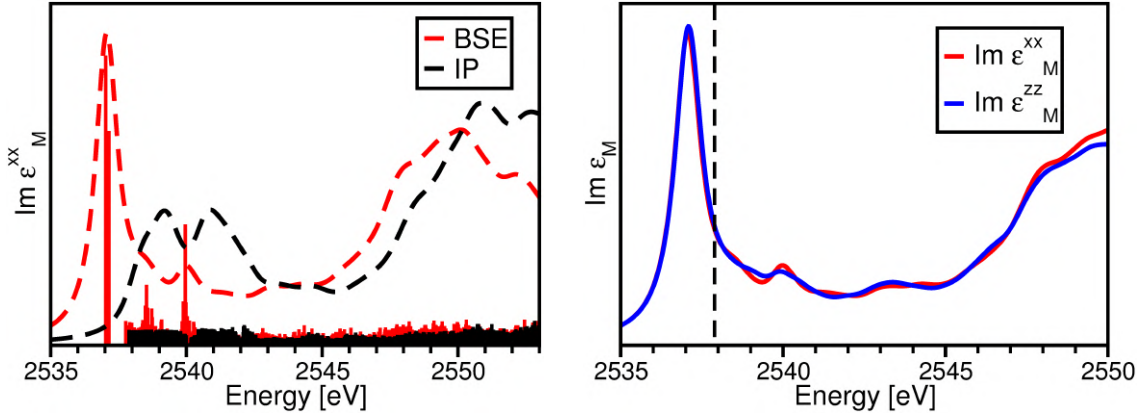
Figure 10.2: Left: excitation energies (vertical bars) and their oscillator strengths (height of the bars) from the solution of the BSE (red) and in the IP approximation (black). The resulting absorption spectra are displayed for reference. Right: Inequivalent components the dielectric tensor. The dotted line indicates the onset of IP absorption.
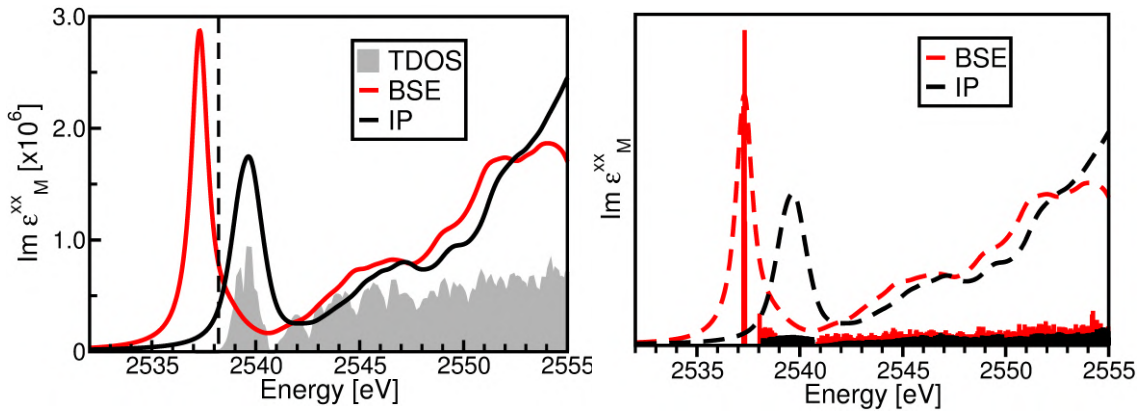
Figure 10.3: Pb M_4 edge absorption spectrum for PbI_2 from the solution of the BSE (red) and in the IP approximation (black). For comparison, the total DOS is shown in the left panel, while the right panel indicates the excitation energies (vertical bars) and their oscillator strengths (height of the bars). The resulting spectra are shown for reference.

In summary, the Pb M_4 edge spectrum of $MAPbI_3$ displays a strong excitonic peak formed by the transition into the Pb d-states at the edge of the conduction band. The bound excitons have binding energies of up to 863 meV. A smaller second peak is formed by transitions into the Pb d-states which are hybridized with states of the organic compound. At higher energies, absorption in the broad Pb f-band is observed. Calculations neglecting the exchange interaction in the BSE Hamiltonian, i.e. $H^x = 0$ in Eq. (4.20) indicate, that the the strong exciton is formed by the screened core hole potential. Comparison with the spectrum of PbI_2 also shows a strongly bound exciton with a comparable binding energy of 953 meV. The high-energy transitions into Pb f-states are also very similar between the two compounds. A significant difference is that in the PbI_2 spectrum, no second peak occurs, which further indicates the contribution from the organic compound to this peak.

11. Conclusions and Outlook

In the second part of this thesis, the electronic structure and core-level spectra of the hybrid organic-inorganic perovskite $MAPbI_3$ were calculated. All calculations were performed for the high-temperature pseudocubic phase, using the all-electron (L)APW+LO implementation in **exciting**. The study of the electronic structure was focused on the unoccupied region of the electronic structure, since this energy region is probed in x-ray absorption spectroscopy. The careful determination of atomic contributions to different bands was used in the analysis of the core spectra. Results of this thesis for the electronic structure and the band structure are in good agreement with previous calculations.

X-ray absorption spectra were calculated using an implementation of the all-electron many body approach to core-level excitations. Excitations from the I $L_{2,3}$ edge as well as from the Pb $M_{4,5}$ edge were studied. Results are obtained from the solution of the BSE, as well as in the independent-particle approximation, thus allowing for an analysis of excitonic effects. Results were compared to the corresponding spectra of PbI_2.

For the I $L_{2,3}$ edge, it was found that the subedges can be calculated separately, due to the strong spin-orbit coupling between the I $2p_{1/2}$ and I $2p_{3/2}$ states. The two subedges show identical spectral features, such that the analysis was limited to the I L_2 edge. Two different kinds of transitions were observed: In the low energy region, transitions to the iodide sp-hybridized band dominate the spectrum, at higher energies the spectrum is formed by the transitions to the broad iodide d-band. Comparison to calculations in the IP approximation show that while the electron-hole interaction induces an overall redshift of the spectrum, the redistribution of the spectral feature is minor. Bound excitons with binding energies of about 448 meV are observed. Comparison with the I L_2 edge spectrum of the binary compound PbI_2 show that the minor differences in the spectra are due to differences in the DOS. Overall, the spectral features are very similar, even for the bound excitons. Bound excitons with binding energy of 448 meV are observed in PbI_2.

The Pb $M_{4,5}$ edge spectrum for $MAPbI_3$ can also —as in the case of the I $L_{2,3}$ edge spectrum— be separated in the independent subedges, due to the strong spin-orbit coupling between the core states. In the Pb M_4 edge spectrum, one observe a strong excitonic peak with binding energy of 863 meV. A second, weaker peak at higher energies is observed, which also has excitonic character. The high-energy part of the spectrum is formed by transitions into the lead f-band. Comparison with calculations in the IP approximation confirms the excitonic character of the first peaks. Transitions at higher energies are well described in the IP approximation. The exchange interaction is negligible in this spectrum, indicating that local field effects are insignifcant. Comparison of the spectrum to that of PbI_2 indicates contributions of the organic compound to the second peak at 2540 eV, as this peak does not occur in PbI_2. A strong excitonic peak is observed in PbI_2 with binding energy of 953 meV.

The work presented here is the first *ab initio* study of the core excitations of this hybrid organic-inorganic perovskite. We intent to extend the study to other materials in the family of hybrid perovskite ABX_3, where A is a organic group, such as CH_3NH_3 or NH_4, B is a metal, usually Pb or Sn, and X is a halide, typically I or Br. Further studies will also investigate the nature of the bound excitons, especially in the Pb $M_{4,5}$ edge spectra. Comparison with experimental results are planned as well.

Appendix A

This appendix supplements Chapters 9 and 10, where the $L_{2,3}$ edge and $M_{4,5}$ edge absorption spectra of MAPbI$_3$ and PbI$_2$ are discussed. Absorption spectra calculated within the BSE formalism are converged with respect to the $\mathbf{k}$-grid, the cut-off value $|\mathbf{G} + \mathbf{q}|_{max}$ for the inclusion of local field effects, the cut-off $R_{MT}G_{max}$ for the basis set and the number of empty states N_{empty} in the RPA screening.

Convergence calculations were performed using only a limited number of unoccupied states in the BSE Hamiltonian. Since the Hamiltonian sizes scales to fourth order with the number of unoccupied states, as well as with the number of $\mathbf{k}$-points, calculations with bigger numbers of states are computitionally costly. As such, the spectra shown below only show the absorption behavior close to the absorption onset. For all convergence tests, the spin-orbit coupling of the core states was neglected. All calculations, irrespective of the edge, are found to converge quickly with the parameter $R_{MT}G_{max}$, such that the converged ground state value ($R_{MT}G_{max} = 4.7$ for MAPbI$_3$ and $R_{MT}G_{max} = 11.5$ for PbI$_2$) are used in the BSE calculations. For all calculations, 100 unoccupied state in the RPA screening yields converged results.

The convergence of the MAPbI$_3$ I $L_{2,3}$ edge absorption spectrum with respect to $|\mathbf{G} + \mathbf{q}|_{max}$ and the $\mathbf{k}$-grid is shown in Figs. (1a) and (1b), respectively. The convergence of the $M_{4,5}$ edge absorption spectra with respect to these parameters is shown in Fig. (2). The convergence of the PbI$_2$ $L_{2,3}$ and $M_{4,5}$ edge spectra was performed as well, the results of these calculations are displayed in Fig. (3) and (4), respectively.

Figure 1: *Convergence of the I $L_{2,3}$ absorption spectrum of MAPbI$_3$ with respect to a) $|\mathbf{G} + \mathbf{q}|_{max}$ and b) the number of $\mathbf{k}$-points. Calculations were performed neglecting the spin-orbit coupling of the I $2p$-states.*
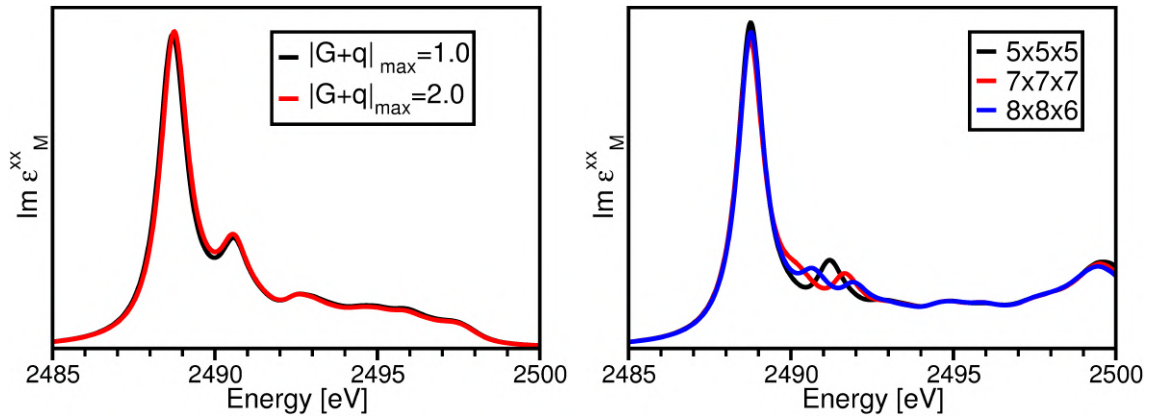
Figure 2: *Convergence of the Pb M_{45} spectrum for MAPbI$_3$ with respect to a)$|\mathbf{G} + \mathbf{q}|_{max}$ and b) the number of $\mathbf{k}$-points. In these calculations, the spin-orbit coupling of the core states is neglected. The xx-component of the dielectric tensor is shown. For computitional details, see the text.*
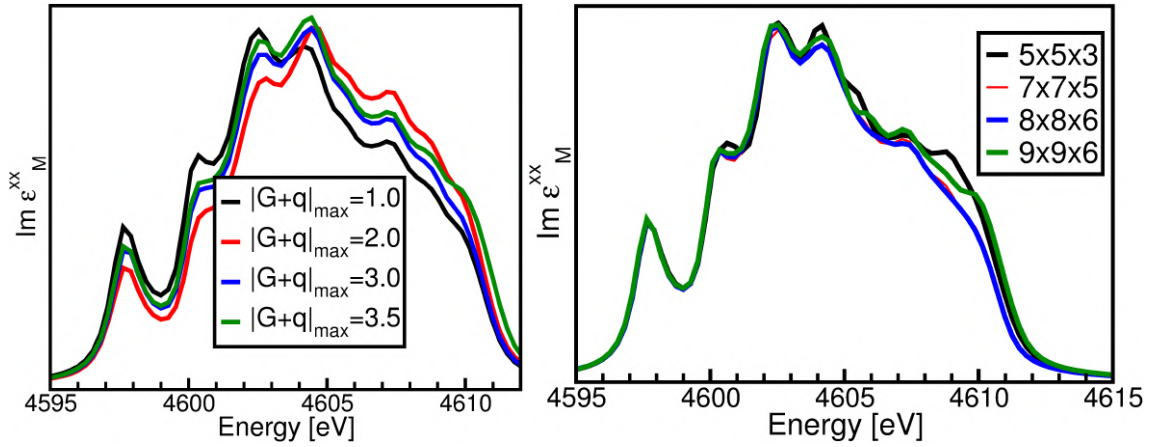
Figure 3: *Convergence of the I $L_{2,3}$ absorption spectrum of PbI$_2$ with respect to a) $|\mathbf{G} + \mathbf{q}|_{max}$ and b) the number of $\mathbf{k}$-points. Calculations were performed neglecting the spin-orbit coupling of the I $2p$-states.*
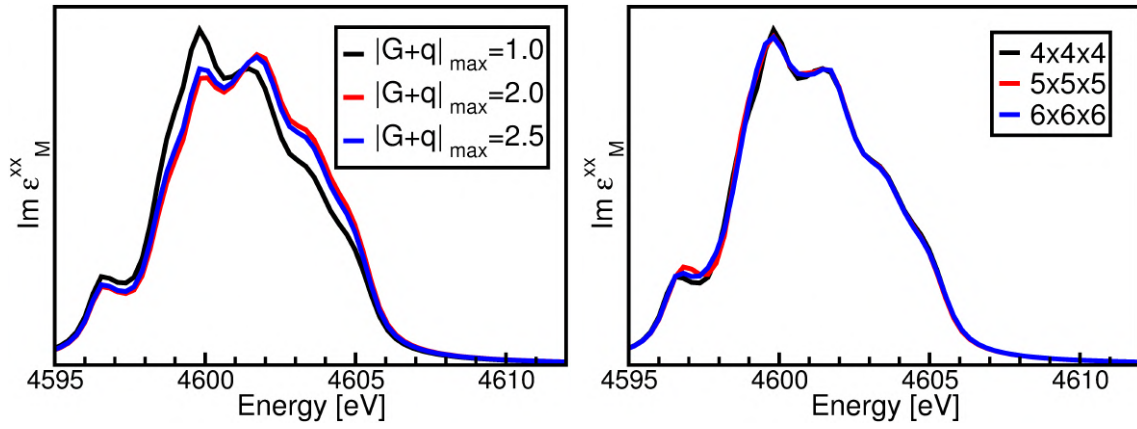

Figure 4: *Convergence of the I $M_{4,5}$ absorption spectrum of PbI$_2$ with respect to a) $|\mathbf{G} + \mathbf{q}|_{max}$ and b) the number of $\mathbf{k}$-points. Calculations were performed neglecting the spin-orbit coupling of the I $2p$-states.*
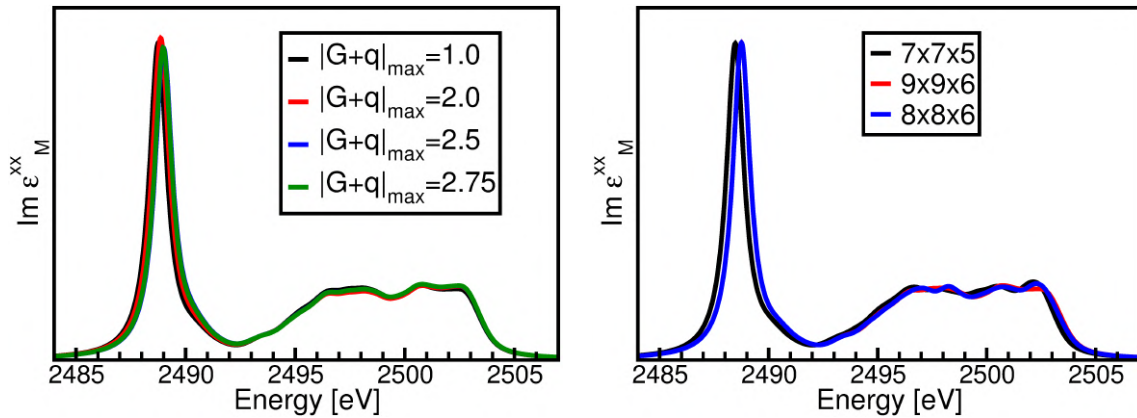
Appendix B

In this appendix, all Fortran90 subroutines and modules, which were added to the **exciting** package in the framework of this thesis, are listed. The implementation of core-level spectra is integrated into the existing exited-state (`xs`) part of the package. For more details of the implementation of BSE calculations for optical absorption spectra, see [65][58]. Whenever subroutines are modifications of existing ones, this is explicitly stated below.

The diagonalization of the BSE Hamiltonian and the construction of the spectrum from the BSE eigenvalues and -vectors is performed in the subroutine `xas`. The matrix elements of the screened Coulomb interaction and the exchange Coulomb interaction are constructed in `xas_scrcoulint` and `xas_exccoulint`, respectively. Other subroutines and modules provide the planewave matrix elements needed for the matrix elements, as well as the momentum matrix elements needed for the oscillator strength of the excitons.

---

xas (Source File: xas.f90)

INTERFACE:

```
Subroutine xas
```

USES:

```
        Use modinput
        Use modmain
        use modmpi
        Use modxs
        Use m_genwgrid
        Use m_getpmatxas
        Use m_genfilname
        Use m_getunit
        Use m_genloss
        Use m_gensigma
        Use m_gensumrls
        Use m_writeeps
        Use m_writeloss
        Use m_writesigma
        Use m_writesumrls
    Use modxas
```

DESCRIPTION:
nteraction

Solves the Bethe-Salpeter equation (BSE). The BSE is treated as equivalent effective eigenvalue problem (thanks to the spectral theorem that can be applied to the original BSE in the case of a statically screened Coulomb interaction). The effective BSE-Hamiltonian

consists of three parts originating from different sources. It reads

$$H^{\mathrm{eff}} = H^{\mathrm{diag}} + H^{\mathrm{x}} + H^{\mathrm{c}},$$

where H^{diag} is the diagonal part stemming from the independent particle transitions, H^{x} denotes the exchange-term caused by the unscreened (bare) Coulomb interaction, whereas H^{c} accounts for the particle-hole correlations and is originating from the screened Coulomb interaction. For the purpose of describing independent particle transitions with the BSE only the diagonal term is referred to:

$$H^{\mathrm{eff}} = H^{\mathrm{diag}}.$$

By neglecting the correlation part in the effective Hamiltonian we arrive at the *random phase approximation* (RPA)

$$H^{\mathrm{eff}} = H^{\mathrm{diag}} + H^{\mathrm{x}}.$$

The equation of the eigenvalue problem is given by

$$\sum_{v'c'\mathbf{k}'} H^{\mathrm{eff}}_{vc\mathbf{k},v'c'\mathbf{k}'} A^{\lambda}_{v'c'\mathbf{k}'} = \varepsilon_{\lambda} A^{\lambda}_{vc\mathbf{k}}.$$

For the diagonalization of the Hamiltonian, a LAPACK-routine (`zheevx`) is invoked to obtain the eigenvalues ε_{λ} and eigenvectors $A^{\lambda}_{vc\mathbf{k}}$ (alternatively, a time-evolution method shall be implemented to obtain the macroscopic dielectric function directly). Consequently, the transition amplitudes t_{λ} are calculated according to

$$t^{i}_{\lambda} = \left| \sum_{vc\mathbf{k}} A^{\lambda}_{vc\mathbf{k}} \frac{p^{i}_{vc\mathbf{k}}}{\varepsilon_{c\mathbf{k}} - \varepsilon_{v\mathbf{k}}} \right|^{2}.$$

Here, the index i labels the polarization and the matrix elements $p^{i}_{vc\mathbf{k}}$ are the ones for the i-th component of the momentum operator in Cartesian coordinates. The macroscopic dielectric function (MDF) is obtained by the realation

$$\mathrm{Im}\,\epsilon^{i}_{\mathrm{M}}(\omega) = \frac{8\pi^{2}}{V} \sum_{\lambda} t^{i}_{\lambda} \delta(\omega - \varepsilon_{\lambda} + \Delta),$$

where $\epsilon^{i}_{\mathrm{M}}$ is the MDF for the i-th polarization, V denotes the crystal volume and Δ is a constant shift of the conduction bands (scissors shift). The delta-function in the latter expression is convoluted with a (symmetrized) Lorentzian.(All parts of the documentation written by S. Sagmeister are part of the author's PhD-thesis.) For the case of core-level excitations, spinor description of core and conduction states are used. Note that therefore the Hamiltonian does NOT decouple in singlet and triplet excitations and the Hamiltonian has the form provided above. More details can be found in Christian Vorwerk's Master thesis.

REVISION HISTORY:

```
Created June 2008 (S. Sagmeister)
Addition of explicit energy ranges for states below and
    above the Fermi
  level for the treatment of core excitations (using
    local orbitals).
  October 2010 (Weine Olovsson)
Added possibility to compute off-diagonal optical
    components, Dec 2013 (Stefan Kontur, STK)
Adaption to the calculation of core-level excitations,
    June 2015 (Christian Vorwerk)
```

xas_scrcoulint (Source File: xas_scrcoulint.f90)

INTERFACE:

```
Subroutine xas_scrcoulint
```

USES:

```
        Use modmain
        Use modinput
        Use modmpi
        Use modxs
        Use summations
        Use m_xasgauntgen
        Use m_xsgauntgen
        Use m_findgntn0
        Use m_writevars
        Use m_genfilname
        Use m_getunit
        Use modxas
```

DESCRIPTION:

Calculates the direct term of the Bethe-Salpeter Hamiltonian for core excitations.

REVISION HISTORY:

```
    Created June 2008 (S. Sagmeister)
    Addition of explicit energy ranges for states below and
        above the Fermi
      level for the treatment of core excitations (using
        local orbitals).
    October 2010 (Weine Olovsson)
    Application to direct terms between core states and
        conduction states for the
    calculation of X-ray absorption spectroscopy.
        November 2015 (Christian Vorwerk)
```

xas_exccoulint (Source File: xas_exccoulint.F90)

INTERFACE:

```
Subroutine xas_exccoulint
```

USES:

```
        Use modmain
        Use modinput
```

```
Use modmpi
Use modxs
Use ioarray
Use m_xasgauntgen
Use m_xsgauntgen
Use m_findgntn0
Use m_writegqpts
Use m_genfilname
Use m_getunit
Use modxas
```

DESCRIPTION:

Calculates the exchange term of the Bethe-Salpeter Hamiltonian for core excitations.

REVISION HISTORY:

```
Created June 2008 (S. Sagmeister)
Addition of explicit energy ranges for states below and
    above the Fermi
  level for the treatment of core excitations (using
    local orbitals).
  October 2010 (Weine Olovsson)
  Application to exchange terms between core states and
      conduction states for the
  calculation of X-ray absorption spectroscopy.
    November 2015 (Christian Vorwerk)
```

---

ematdirect (Source File: ematdirect.f90)

INTERFACE:

```
Subroutine ematdirect (iq, ik)
```

INPUT/OUTPUT PARAMETERS:

```
iq        : q-point position (in,integer)
ik        : k-point position (in,integer)
```

DESCRIPTION:

Calculates the plane wave matrix elements $M_{cc'\mathbf{k}}(\mathbf{q} + \mathbf{G})$ between two core states and $M_{uu'\mathbf{k}}(\mathbf{q} + \mathbf{G})$ between two conduction states. The matrix elements are used for the construction of the direct terms in the BSE Hamiltonian (see xas.f90).

USES:

```
Use modmain
Use modinput
Use modxs
```

```
        Use modmpi
        Use m_putemat
        Use modxas
        Implicit None
```

REVISION HISTORY:

```
    Created June 2015 by C. Vorwerk
```

---

ematex (Source File: ematex.f90)

INTERFACE:

```
 Subroutine ematex(iq, ik)
```

USES:

```
        Use modmain
        Use modinput
        Use modxs
        Use modmpi
        Use m_putemat
        Use modxas
```

INPUT/OUTPUT PARAMETERS:

```
    iq : q-point position (in,integer)
    ik : k-point position (in,integer)
```

DESCRIPTION:

Calculates Planewave Matrix elements for the exchange term of the BSE Hamiltonian.

REVISION HISTORY:

```
    Based on the subroutine ematqk1.F90
    Created November 2015 (Christian Vorwerk)
```

---

genxioo (Source File: genxioo.f90)

INTERFACE:

```
 Subroutine genxioo (iq, ik, xi)
```

USES:

```
        Use mod_constants
        Use mod_eigenvalue_occupancy
        Use mod_misc
        Use mod_Gkvector
```

```
        Use mod_APW_LO
        Use mod_Gvector
        Use mod_kpoint
        Use modinput
        Use modmpi
        Use modxs
        Use summations
        Use m_getapwcmt
        Use m_getlocmt
        Use m_putemat
        Use m_emattim
        Use m_getunit
        Use m_genfilname
        use modmain
        use modxas
#ifdef USEOMP
        use omp_lib
#endif
```

INPUT/OUTPUT PARAMETERS:

```
    ik : k-point position (in,integer)
    iq : q-point position (in,integer)
    xi : planewave matrix element (complex(nxas, nxas, ngq(
        iq)), out)
```

DESCRIPTION:

Calculates Planewave Matrix elements $M_{\mu\mu'}(\mathbf{q} + \mathbf{G})$ between two core states. See Vorwerk's Master thesis for more details.

REVISION HISTORY:

```
    Based on the subroutine ematqk.F90
    Created November 2015 (Christian Vorwerk)
```

---

genxiou (Source File: genxiou.f90)

INTERFACE:

```
 Subroutine genxiou (iq, ik, xi)
```

USES:

```
        Use mod_constants
        Use mod_eigenvalue_occupancy
        Use mod_misc
        Use mod_Gkvector
        Use mod_APW_LO
        Use mod_Gvector
```

```
        Use mod_kpoint
        Use modinput
        Use modmpi
        Use modxs
        Use summations
        Use m_getapwcmt
        Use m_getlocmt
        Use m_putemat
        Use m_emattim
        Use m_getunit
        Use m_genfilname
        use modmain
        Use modxas
 #ifdef USEOMP
        use omp_lib
 #endif
```

INPUT/OUTPUT PARAMETERS:

```
    ik : k-point position (in,integer)
    iq : q-point position (in,integer)
    xi : planewave matrix element (complex, out)
```

DESCRIPTION:

Calculates Planewave Matrix elements $M_{\mu\mathbf{k}}(\mathbf{q}+\mathbf{G})$ between a core state and a conduction state. See Vorwerk's Master thesis for more details.

REVISION HISTORY:

```
    Based on the subroutine ematqk.F90
    Created November 2015 (Christian Vorwerk)
```

---

ematradoo (Source File: ematradoo.f90)

INTERFACE:

```
 Subroutine ematradoo (iq,ik, igq, integral)
```

USES:

```
  Use modmain
  Use modinput
  Use modxs
  Use m_getunit
  Use modxas
```

INPUT/OUTPUT PARAMETERS:

```
    iq : q-point position (in,integer)
    ik : k-point position (in,integer)
```

```
igq : (q+G)-point position (in,integer)
integral : radial planewave integral
        (out, complex(lmaxemat+1,nxas,nxas))
```

DESCRIPTION:

Calculates the radial integral part $R^l_{\mu\mu'}(\mathbf{q} + \mathbf{G})$ of the planewave matrix element between two core states. See Vorwerk's Master thesis for more details.

REVISION HISTORY:

```
Based on the subroutine ematqk.F90
Created November 2015 (Christian Vorwerk)
```

---

ematradou (Source File: ematradou.f90)

INTERFACE:

```
Subroutine ematradou (iq,ik, igq, ngp, apwalm, evecfvo, integral)
```

USES:

```
Use modmain
Use modinput
Use modxs
Use m_getunit
Use modxas
```

INPUT/OUTPUT PARAMETERS:

```
  ik : k-point position (in,integer)
 ngp : number of G+p-vectors (in,integer)
apwalm : APW matching coefficients
        (in,complex(ngkmax,apwordmax,lmmaxapw,natmtot))
evecfvo : first-variational eigenvector (in,complex(
   nmatmax))
integral : radial planewave integral
        (out, complex(lmaxemat+1,lmmaxapw,nxas,sta2:sto
           2))
```

DESCRIPTION:

Calculates the radial integral part $R^{ll'}_{\mu m(\mathbf{k}+\mathbf{q})}(\mathbf{q} + \mathbf{G})$ of the planewave matrix element between a core state and a conduction state. See Vorwerk's Master thesis for more details.

REVISION HISTORY:

```
Based on the subroutine ematqk.F90
Created November 2015 (Christian Vorwerk)
```

---

ematsumoo (Source File: ematsumoo.f90)

INTERFACE:

```
Subroutine ematsumoo (iq,ik, igq, integral, xi)
```

USES:

```
Use modmain
Use modinput
Use modxs
Use modxas
```

INPUT/OUTPUT PARAMETERS:

```
iq : q-point position (in,integer)
ik : k-point position (in,integer)
igq  : (q+G)-point position (in, integer)
integral : radial planewave integral
        (in, complex(lmaxemat+1,nxas,nxas))
  xi : planewave matrix element (inout,complex(nxas,
     sta2:sto2, ngq(iq))
```

DESCRIPTION:

Calculates planewave matrix elements between two core states, using the radial integrals. Fore more information, see Christian Vorwerk's Master thesis, Eq. (5.16). **REVISION HISTORY:**

```
Based on the subroutine ematqkgmt.F90
Created November 2015 (Christian Vorwerk)
```

---

ematsumou (Source File: ematsumou.f90)

INTERFACE:

```
Subroutine ematsumou (iq,ik, igq, integral, xi)
```

USES:

```
Use modmain
Use modinput
Use modxs
Use m_getunit
Use modxas
```

INPUT/OUTPUT PARAMETERS:

```
iq : q-point position (in,integer)
ik : k-point position (in,integer)
igq  : (q+G)-point position (in, integer)
integral : radial planewave integral
```

```
        (in, complex(lmaxemat+1,lmmaxapw,nxas,sta2:sto
           2))
   xi : planewave matrix element (inout,complex(nxas,
       sta2:sto2, ngq(iq))
```

DESCRIPTION:

Calculates planewave matrix elements between a core and a conduction state, using the radial integrals. Fore more information, see Christian Vorwerk's Master thesis, Eq. (5.20).

REVISION HISTORY:

```
    Based on the subroutine ematqkgmt.F90
    Created November 2015 (Christian Vorwerk)
```

---

xasinit (Source File: xasinit.f90)

INTERFACE:

```
 subroutine xasinit
```

DESCRIPTION:

This is the main initialization subroutine of the BSE-XAS program.

USES:

```
  Use modmain
  Use modinput
  Use modxs
  Use modxas
  Implicit none
  Integer :: is, ist, m, ic, ias, l, ir, ia, k
```

REVISION HISTORY:

```
  Created June 2015 by C. Vorwerk
```

Module Interface m_xasgauntgen (Source File: xasgauntgen.f90)

Provides the subroutine to calculate the spin Gaunt coefficients needed in the caluclation of plane wave matrix elements between core and conduction states. More details are provided in Christian Vorwerk's Master thesis.

REVISION HISTORY:

```
    Created JUNE 2015  (Christian Vorwerk)
```

genpmatcorxs (Source File: genpmatcorxs.f90)

INTERFACE:

```
subroutine genpmatcorxs(ik,ngp,apwalm,evecfv,evecsv,pmatc)
```

USES:

```
    use modinput
    use modmain
    use modxas
```

INPUT/OUTPUT PARAMETERS:

```
    ik : k-point position (in,integer)
    ngp : number of G+p-vectors (in,integer)
    apwalm : APW matching coefficients
            (in,complex(ngkmax,apwordmax,lmmaxapw,natmtot))
    evecfv : first-variational eigenvector (in,complex(
        nmatmax,nstfv))
    evecsv : second-variational eigenvectors (in,complex(
        nstsv,nstsv))
    pmatc : momentum matrix elements (out,complex(3,ncg,
        nstsv))
```

DESCRIPTION:

Calculates the momentum matrix elements between a core state and a conduction state.

REVISION HISTORY:

```
    Created August 2006 (RGA)
    Revisited June 2011 (DIN)
 Adjusted to core states November 2015 (Christian Vorwerk)
```

Module Interface modxas (Source File: modxas.f90)

Contains additional global variables required for XAS calculations within the BSE EX-CITING code.

REVISION HISTORY:

```
    Created JUNE 2015 (Christian Vorwerk)
```

Module Interface m_getpmatxas (Source File: getpmatxas.f90)

Provides Subroutines to obtain the momentum matrix elements needed for BSE from file.

Bibliography

[1] AHMED, Towfiq ; VORAKIAT, C. L. ; SALIM, T. ; LAM, Y. M. ; CHIA, Elbert E. M. ; ZHU, Jian-Xin: Optical properties of organometallic perovskite: An ab initio study using relativistic GW correction and Bethe-Salpeter equation. In: *EPL (Europhysics Letters)* 108 (2014), Nr. 6, 67015. `http://stacks.iop.org/0295-5075/108/i=6/a=67015`

[2] ANDERSEN, O. K.: Linear methods in band theory. In: *Phys. Rev. B* 12 (1975), Oct, 3060–3083. `http://dx.doi.org/10.1103/PhysRevB.12.3060`. – DOI 10.1103/PhysRevB.12.3060

[3] ANKUDINOV, A. L. ; NESVIZHSKII, A. I. ; REHR, J. J.: Dynamic screening effects in x-ray absorption spectra. In: *Phys. Rev. B* 67 (2003), Mar, 115120. `http://dx.doi.org/10.1103/PhysRevB.67.115120`. – DOI 10.1103/PhysRevB.67.115120

[4] BACH U. ; LUPO D. ; COMTE P. ; MOSER J. E. ; WEISSORTEL F. ; SALBECK J. ; SPREITZER H. ; GRATZEL M.: Solid-state dye-sensitized mesoporous TiO2 solar cells with high photon-to-electron conversion efficiencies. In: *Nature* 395 (1998), oct, Nr. 6702, S. 583–585. `http://dx.doi.org/http://dx.doi.org/10.1038/26936`. – DOI http://dx.doi.org/10.1038/26936. – ISSN 0028–0836. – 10.1038/26936

[5] BAIKIE, Tom ; FANG, Yanan ; KADRO, Jeannette M. ; SCHREYER, Martin ; WEI, Fengxia ; MHAISALKAR, Subodh G. ; GRAETZEL, Michael ; WHITE, Tim J.: Synthesis and crystal chemistry of the hybrid perovskite (CH3NH3)PbI3 for solid-state sensitised solar cell applications. In: *J. Mater. Chem. A* 1 (2013), 5628-5641. `http://dx.doi.org/10.1039/C3TA10518K`. – DOI 10.1039/C3TA10518K

[6] BAIKIE, Tom ; FANG, Yanan ; KADRO, Jeannette M. ; SCHREYER, Martin ; WEI, Fengxia ; MHAISALKAR, Subodh G. ; GRAETZEL, Michael ; WHITE, Tim J.: Synthesis and crystal chemistry of the hybrid perovskite (CH3NH3)PbI3 for solid-state sensitised solar cell applications. In: *J. Mater. Chem. A* 1 (2013), 5628-5641. `http://dx.doi.org/10.1039/C3TA10518K`. – DOI 10.1039/C3TA10518K

[7] BETZINGER, Markus: *Efficient Implementation of the Non-Local Exchange Potential within the FLAPW Method*, Rheinisch-Westfaelische Technische Hochschule Aachen, Diplomarbeit, 2007

[8] BISQUERT, Juan: The Swift Surge of Perovskite Photovoltaics. In: *The Journal of Physical Chemistry Letters* 4 (2013), Nr. 15, 2597-2598. `http://dx.doi.org/10.1021/jz401435d`. – DOI 10.1021/jz401435d

[9] BLAHA, P. ; SCHWARZ, K. ; MADSEN, G. K. H. ; KVASNICKA, D. ; LUITZ, J.: *WIEN2K, An Augmented Plane Wave + Local Orbitals Program for Calculating Crystal Properties*. Karlheinz Schwarz, Techn. Universität Wien, Austria, 2001

[10] BORRIELLO, Ivo ; CANTELE, Giovanni ; NINNO, Domenico: *Ab initio* investigation of hybrid organic-inorganic perovskites based on tin halides. In: *Phys. Rev. B* 77 (2008), Jun, 235214. `http://dx.doi.org/10.1103/PhysRevB.77.235214`. – DOI 10.1103/PhysRevB.77.235214

[11] BRIVIO, Federico ; BUTLER, Keith T. ; WALSH, Aron ; SCHILFGAARDE, Mark van: Relativistic quasiparticle self-consistent electronic structure of hybrid halide perovskite photovoltaic absorbers. In: *Phys. Rev. B* 89 (2014), Apr, 155204. http://dx.doi.org/10.1103/PhysRevB.89.155204. – DOI 10.1103/PhysRevB.89.155204

[12] BRIVIO, Federico ; WALKER, Alison B. ; WALSH, Aron: Structural and electronic properties of hybrid perovskites for high-efficiency thin-film photovoltaics from first-principles. In: *APL Mater.* 1 (2013), Nr. 4. http://dx.doi.org/http://dx.doi.org/10.1063/1.4824147. – DOI http://dx.doi.org/10.1063/1.4824147

[13] BRIVIO, Federico ; WALKER, Alison B. ; WALSH, Aron: Structural and electronic properties of hybrid perovskites for high-efficiency thin-film photovoltaics from first-principles. In: *APL Mater.* 1 (2013), Nr. 4. http://dx.doi.org/http://dx.doi.org/10.1063/1.4824147. – DOI http://dx.doi.org/10.1063/1.4824147

[14] BURKE, Kieron ; WERSCHNIK, Jan ; GROSS, E. K. U.: Time-dependent density functional theory: Past, present, and future. In: *The Journal of Chemical Physics* 123 (2005), Nr. 6. http://dx.doi.org/http://dx.doi.org/10.1063/1.1904586. – DOI http://dx.doi.org/10.1063/1.1904586

[15] CHEN, C.-C. ; SENTEF, M. ; KUNG, Y. F. ; JIA, C. J. ; THOMALE, R. ; MORITZ, B. ; KAMPF, A. P. ; DEVEREAUX, T. P.: Doping evolution of the oxygen K-edge x-ray absorption spectra of cuprate superconductors using a three-orbital Hubbard model. In: *Phys. Rev. B* 87 (2013), Apr, 165144. http://dx.doi.org/10.1103/PhysRevB.87.165144. – DOI 10.1103/PhysRevB.87.165144

[16] DUSCHER, G. ; BUCZKO, R. ; PENNYCOOK, S.J. ; PANTELIDES, S.T.: Core-hole effects on energy-loss near-edge structure. In: *Ultramicroscopy* 86 (2001), Nr. 3–4, 355 - 362. http://dx.doi.org/http://dx.doi.org/10.1016/S0304-3991(00)00126-1. – DOI http://dx.doi.org/10.1016/S0304–3991(00)00126–1. – ISSN 0304–3991. – International Symposium on Spectroscopy of Materials

[17] FILIP, Marina R. ; GIUSTINO, Feliciano: GW quasiparticle band gap of the hybrid organic-inorganic perovskite $CH_3NH_3PbI_3$: Effect of spin-orbit interaction, semicore electrons, and self-consistency. In: *Phys. Rev. B* 90 (2014), Dec, 245145. http://dx.doi.org/10.1103/PhysRevB.90.245145. – DOI 10.1103/PhysRevB.90.245145

[18] FRIEDRICH, Christoph ; SCHINDLMAYER, Arno: Many-Body Perturbation Theory: The GW approximation. In: J. GROTENDORST, D. M. S. Bluegel B. S. Bluegel (Hrsg.): *Computitional Nanoscience: Do It Yourself!* John von Neumann Institute for Computing, Juelich, 2006

[19] GAO, Weiwei ; GAO, Xiang ; ABTEW, Tesfaye A. ; SUN, Yi-Yang ; ZHANG, Shengbai ; ZHANG, Peihong: Quasiparticle band gap of organic-inorganic hybrid perovskites: Crystal structure, spin-orbit coupling, and self-energy effects. In: *Phys. Rev. B* 93 (2016), Feb, 085202. http://dx.doi.org/10.1103/PhysRevB.93.085202. – DOI 10.1103/PhysRevB.93.085202

[20] GILMORE, K. ; VINSON, John ; SHIRLEY, E.L. ; PRENDERGAST, D. ; PEM-MARAJU, C.D. ; KAS, J.J. ; VILA, F.D. ; REHR, J.J.: Efficient implementation of core-excitation Bethe–Salpeter equation calculations. In: *Computer Physics Communications* 197 (2015), 109 - 117. `http://dx.doi.org/http://dx.doi.org/10.1016/j.cpc.2015.08.014.` – DOI http://dx.doi.org/10.1016/j.cpc.2015.08.014. – ISSN 0010–4655

[21] GLAZER, A. M.: The classification of tilted octahedra in perovskites. In: *Acta Crystallographica Section B* 28 (1972), Nr. 11, 3384–3392. `http://dx.doi.org/10.1107/S0567740872007976.` – DOI 10.1107/S0567740872007976. – ISSN 1600–5740

[22] GONZE, X. ; AMADON, B. ; ANGLADE, P.-M. ; BEUKEN, J.-M. ; BOTTIN, F. ; BOULANGER, P. ; BRUNEVAL, F. ; CALISTE, D. ; CARACAS, R. ; CÔTÉ, M. ; DEUTSCH, T. ; GENOVESE, L. ; GHOSEZ, Ph. ; GIANTOMASSI, M. ; GOEDECKER, S. ; HAMANN, D.R. ; HERMET, P. ; JOLLET, F. ; JOMARD, G. ; LEROUX, S. ; MANCINI, M. ; MAZEVET, S. ; OLIVEIRA, M.J.T. ; ONIDA, G. ; POUILLON, Y. ; RANGEL, T. ; RIGNANESE, G.-M. ; SANGALLI, D. ; SHALTAF, R. ; TORRENT, M. ; VERSTRAETE, M.J. ; ZERAH, G. ; ZWANZIGER, J.W.: ABINIT: First-principles approach to material and nanosystem properties. In: *Computer Physics Communications* 180 (2009), Nr. 12, 2582 - 2615. `http://dx.doi.org/http://dx.doi.org/10.1016/j.cpc.2009.07.007.` – DOI http://dx.doi.org/10.1016/j.cpc.2009.07.007. – ISSN 0010–4655. – 40 {YEARS} {OF} CPC: A celebratory issue focused on quality software for high performance, grid and novel computing architectures

[23] GULANS, Andris ; KONTUR, Stefan ; MEISENBICHLER, Christian ; NABOK, Dmitrii ; PAVONE, Pasquale ; RIGAMONTI, Santiago ; SAGMEISTER, Stephan ; WERNER, Ute ; DRAXL, Claudia: exciting: a full-potential all-electron package implementing density-functional theory and many-body perturbation theory. In: *Journal of Physics: Condensed Matter* 26 (2014), Nr. 36, 363202. `http://stacks.iop.org/0953-8984/26/i=36/a=363202`

[24] HAGFELDT, Anders ; BOSCHLOO, Gerrit ; SUN, Licheng ; KLOO, Lars ; PETTERSSON, Henrik: Dye-Sensitized Solar Cells. In: *Chemical Reviews* 110 (2010), Nr. 11, 6595-6663. `http://dx.doi.org/10.1021/cr900356p.` – DOI 10.1021/cr900356p. – PMID: 20831177

[25] HEDIN, Lars ; LUNDQVIST, Stig: Effects of Electron-Electron and Electron-Phonon Interactions on the One-Electron States of Solids. Version: 1970. `http://dx.doi.org/10.1016/S0081-1947(08)60615-3.` Academic Press, 1970. – DOI 10.1016/S0081–1947(08)60615–3. – ISSN 0081–1947, 1 - 181

[26] HJALMARSON, Harold P. ; BÜTTNER, Helmut ; DOW, John D.: Theory of core excitons. In: *Phys. Rev. B* 24 (1981), Nov, 6010–6019. `http://dx.doi.org/10.1103/PhysRevB.24.6010.` – DOI 10.1103/PhysRevB.24.6010

[27] HOHENBERG, P. ; KOHN, W.: Inhomogeneous Electron Gas. In: *Phys. Rev.* 136 (1964), Nov, B864–B871. `http://dx.doi.org/10.1103/PhysRev.136.B864.` – DOI 10.1103/PhysRev.136.B864

[28] IKENO, Hidekazu ; TANAKA, Isao: Effects of Breit interaction on the $L_{2,3}$ x-ray absorption near-edge structures of $3d$ transition metals. In: *Phys. Rev. B* 77 (2008),

Feb, 075127. `http://dx.doi.org/10.1103/PhysRevB.77.075127`. – DOI 10.1103/PhysRevB.77.075127

[29] JAOUEN, M. ; HUG, G. ; RAVEL, B. ; ANKUDINOV, A. L. ; REHR, J. J.: Polarisation effects in hexagonal boron nitride near-edge structure: A real-space multiple scattering approach. In: *EPL (Europhysics Letters)* 49 (2000), Nr. 3, 343. `http://stacks.iop.org/0295-5075/49/i=3/a=343`

[30] JIANG, N. ; SPENCE, J. C. H.: Core-hole effects on electron energy-loss spectroscopy of Li_2O. In: *Phys. Rev. B* 69 (2004), Mar, 115112. `http://dx.doi.org/10.1103/PhysRevB.69.115112`. – DOI 10.1103/PhysRevB.69.115112

[31] JOHNSON, W.R. ; CHENG, K.T. ; CHEN, M.H.: Chapter 3 Accurate relativistic calculations including {QED} contributions for few-electron systems. Version: 2004. `http://dx.doi.org/http://dx.doi.org/10.1016/S1380-7323(04)80030-X`. In: SCHWERDTFEGER, Peter (Hrsg.): *Relativistic Electronic Structure TheoryPart 2. Applications* Bd. 14. Elsevier, 2004. – DOI http://dx.doi.org/10.1016/S1380–7323(04)80030–X. – ISSN 1380–7323, 120 - 187

[32] KOELLING, D D. ; HARMON, B N.: A technique for relativistic spin-polarised calculations. In: *Journal of Physics C: Solid State Physics* 10 (1977), Nr. 16, 3107. `http://stacks.iop.org/0022-3719/10/i=16/a=019`

[33] KOHN, W. ; SHAM, L. J.: Self-Consistent Equations Including Exchange and Correlation Effects. In: *Phys. Rev.* 140 (1965), Nov, A1133–A1138. `http://dx.doi.org/10.1103/PhysRev.140.A1133`. – DOI 10.1103/PhysRev.140.A1133

[34] KOJIMA, Akihiro ; TESHIMA, Kenjiro ; SHIRAI, Yasuo ; MIYASAKA, Tsutomu: Organometal Halide Perovskites as Visible-Light Sensitizers for Photovoltaic Cells. In: *Journal of the American Chemical Society* 131 (2009), Nr. 17, 6050-6051. `http://dx.doi.org/10.1021/ja809598r`. – DOI 10.1021/ja809598r. – PMID: 19366264

[35] KRONAWITTER, Coleman X. ; KAPILASHRAMI, Mukes ; BAKKE, Jonathan R. ; BENT, Stacey F. ; CHUANG, Cheng-Hao ; PONG, Way-Faung ; GUO, Jinghua ; VAYSSIERES, Lionel ; MAO, Samuel S.: TiO_2-SnO_2:F interfacial electronic structure investigated by soft x-ray absorption spectroscopy. In: *Phys. Rev. B* 85 (2012), Mar, 125109. `http://dx.doi.org/10.1103/PhysRevB.85.125109`. – DOI 10.1103/PhysRevB.85.125109

[36] KRÜGER, Peter: Multichannel multiple scattering calculation of $L_{2,3}$-edge spectra of TiO_2 and $SrTiO_3$: Importance of multiplet coupling and band structure. In: *Phys. Rev. B* 81 (2010), Mar, 125121. `http://dx.doi.org/10.1103/PhysRevB.81.125121`. – DOI 10.1103/PhysRevB.81.125121

[37] LAAN, G. van d.: Polaronic satellites in x-ray-absorption spectra. In: *Phys. Rev. B* 41 (1990), Jun, 12366–12368. `http://dx.doi.org/10.1103/PhysRevB.41.12366`. – DOI 10.1103/PhysRevB.41.12366

[38] LANDMANN, M ; RAULS, E ; SCHMIDT, W G.: The electronic structure and optical response of rutile, anatase and brookite TiO 2. In: *Journal of Physics: Condensed Matter* 24 (2012), Nr. 19, 195503. `http://stacks.iop.org/0953-8984/24/i=19/a=195503`

[39] LASKOWSKI, Robert ; BLAHA, Peter: Understanding the $L_{2,3}$ x-ray absorption spectra of early $3d$ transition elements. In: *Phys. Rev. B* 82 (2010), Nov, 205104. http://dx.doi.org/10.1103/PhysRevB.82.205104. – DOI 10.1103/PhysRevB.82.205104

[40] LEE, Michael M. ; TEUSCHER, Joël ; MIYASAKA, Tsutomu ; MURAKAMI, Takurou N. ; SNAITH, Henry J.: Efficient Hybrid Solar Cells Based on Meso-Superstructured Organometal Halide Perovskites. In: *Science* 338 (2012), Nr. 6107, 643–647. http://dx.doi.org/10.1126/science.1228604. – DOI 10.1126/science.1228604. – ISSN 0036–8075

[41] LENTHE, E. v. ; BAERENDS, E. J. ; SNIJDERS, J. G.: Relativistic regular two-component Hamiltonians. In: *The Journal of Chemical Physics* 99 (1993), Nr. 6, 4597-4610. http://dx.doi.org/http://dx.doi.org/10.1063/1.466059. – DOI http://dx.doi.org/10.1063/1.466059

[42] LUITZ, J. ; MAIER, M. ; HÉBERT, C. ; SCHATTSCHNEIDER, P. ; BLAHA, P. ; SCHWARZ, K. ; JOUFFREY, B.: Partial core hole screening in the Cu L3 edge. In: *Eur. Phys. J. B* 21 (2001), Nr. 3, 363-367. http://dx.doi.org/10.1007/s100510170179. – DOI 10.1007/s100510170179

[43] MAUCHAMP, Vincent ; JAOUEN, Michel ; SCHATTSCHNEIDER, Peter: Core-hole effect in the one-particle approximation revisited from density functional theory. In: *Phys. Rev. B* 79 (2009), Jun, 235106. http://dx.doi.org/10.1103/PhysRevB.79.235106. – DOI 10.1103/PhysRevB.79.235106

[44] MCMEEKIN, David P. ; SADOUGHI, Golnaz ; REHMAN, Waqaas ; EPERON, Giles E. ; SALIBA, Michael ; HÖRANTNER, Maximilian T. ; HAGHIGHIRAD, Amir ; SAKAI, Nobuya ; KORTE, Lars ; RECH, Bernd ; JOHNSTON, Michael B. ; HERZ, Laura M. ; SNAITH, Henry J.: A mixed-cation lead mixed-halide perovskite absorber for tandem solar cells. In: *Science* 351 (2016), Nr. 6269, 151–155. http://dx.doi.org/10.1126/science.aad5845. – DOI 10.1126/science.aad5845. – ISSN 0036–8075

[45] MENÉNDEZ-PROUPIN, E. ; PALACIOS, P. ; WAHNÓN, P. ; CONESA, J. C.: Self-consistent relativistic band structure of the $CH_3NH_3PbI_3$ perovskite. In: *Phys. Rev. B* 90 (2014), Jul, 045207. http://dx.doi.org/10.1103/PhysRevB.90.045207. – DOI 10.1103/PhysRevB.90.045207

[46] MENÉNDEZ-PROUPIN, E. ; PALACIOS, P. ; WAHNÓN, P. ; CONESA, J. C.: Self-consistent relativistic band structure of the $CH_3NH_3PbI_3$ perovskite. In: *Phys. Rev. B* 90 (2014), Jul, 045207. http://dx.doi.org/10.1103/PhysRevB.90.045207. – DOI 10.1103/PhysRevB.90.045207

[47] MIEDEMA, P S. ; IKENO, H ; GROOT, F M F.: First principles multiplet calculations of the calcium L 2, 3 x-ray absorption spectra of CaO and CaF 2. In: *Journal of Physics: Condensed Matter* 23 (2011), Nr. 14, 145501. http://stacks.iop.org/0953-8984/23/i=14/a=145501

[48] MOREAU, P. ; BOUCHER, F. ; GOGLIO, G. ; FOY, D. ; MAUCHAMP, V. ; OUVRARD, G.: Electron energy-loss spectra calculations and experiments as a tool for the identification of a lamellar C_3N_4 compound. In: *Phys. Rev. B* 73 (2006), May, 195111. http://dx.doi.org/10.1103/PhysRevB.73.195111. – DOI 10.1103/PhysRevB.73.195111

[49] MOSCONI, Edoardo ; AMAT, Anna ; NAZEERUDDIN, Md. K. ; GRÄTZEL, Michael ; ANGELIS, Filippo D.: First-Principles Modeling of Mixed Halide Organometal Perovskites for Photovoltaic Applications. In: *The Journal of Physical Chemistry C* 117 (2013), Nr. 27, 13902-13913. `http://dx.doi.org/10.1021/jp4048659`. – DOI 10.1021/jp4048659

[50] OLOVSSON, W. ; TANAKA, I. ; MIZOGUCHI, T. ; PUSCHNIG, P. ; AMBROSCH-DRAXL, C.: All-electron Bethe-Salpeter calculations for shallow-core x-ray absorption near-edge structures. In: *Phys. Rev. B* 79 (2009), Jan, 041102. `http://dx.doi.org/10.1103/PhysRevB.79.041102`. – DOI 10.1103/PhysRevB.79.041102

[51] OLOVSSON, W. ; TANAKA, I. ; MIZOGUCHI, T. ; RADTKE, G. ; PUSCHNIG, P. ; AMBROSCH-DRAXL, C.: Al $L_{2,3}$ edge x-ray absorption spectra in III-V semiconductors: Many-body perturbation theory in comparison with experiment. In: *Phys. Rev. B* 83 (2011), May, 195206. `http://dx.doi.org/10.1103/PhysRevB.83.195206`. – DOI 10.1103/PhysRevB.83.195206

[52] OLOVSSON, W ; TANAKA, I ; PUSCHNIG, P ; AMBROSCH-DRAXL, C: Near-edge structures from first principles all-electron Bethe–Salpeter equation calculations. In: *Journal of Physics: Condensed Matter* 21 (2009), Nr. 10, 104205. `http://stacks.iop.org/0953-8984/21/i=10/a=104205`

[53] ONIDA, Giovanni ; REINING, Lucia ; RUBIO, Angel: Electronic excitations: density-functional versus many-body Green's-function approaches. In: *Rev. Mod. Phys.* 74 (2002), Jun, 601–659. `http://dx.doi.org/10.1103/RevModPhys.74.601`. – DOI 10.1103/RevModPhys.74.601

[54] PAN, Yu-Yun ; SU, Yen-Hsun ; HSU, Chuang-Han ; HUANG, Li-Wen ; KAUN, Chao-Cheng: The electronic structure of organic–inorganic hybrid perovskite solar cell: A first-principles analysis. In: *Computational Materials Science* (2016), -. `http://dx.doi.org/http://dx.doi.org/10.1016/j.commatsci.2015.12.015`. – DOI http://dx.doi.org/10.1016/j.commatsci.2015.12.015. – ISSN 0927–0256

[55] PERDEW, J. P. ; ZUNGER, Alex: Self-interaction correction to density-functional approximations for many-electron systems. In: *Phys. Rev. B* 23 (1981), May, 5048–5079. `http://dx.doi.org/10.1103/PhysRevB.23.5048`. – DOI 10.1103/PhysRevB.23.5048

[56] PERDEW, John P. ; BURKE, Kieron ; ERNZERHOF, Matthias: Generalized Gradient Approximation Made Simple. In: *Phys. Rev. Lett.* 77 (1996), Oct, 3865–3868. `http://dx.doi.org/10.1103/PhysRevLett.77.3865`. – DOI 10.1103/PhysRevLett.77.3865

[57] PERDEW, John P. ; RUZSINSZKY, Adrienn ; CSONKA, Gábor I. ; VYDROV, Oleg A. ; SCUSERIA, Gustavo E. ; CONSTANTIN, Lucian A. ; ZHOU, Xiaolan ; BURKE, Kieron: Restoring the Density-Gradient Expansion for Exchange in Solids and Surfaces. In: *Phys. Rev. Lett.* 100 (2008), Apr, 136406. `http://dx.doi.org/10.1103/PhysRevLett.100.136406`. – DOI 10.1103/PhysRevLett.100.136406

[58] PUSCHNIG, P.: *Excitonic Effects in Organic Semiconductors: An Ab-Initio Study within the LAPW Method*, Karl-Franzens-Universität Graz, Faculty of Natural Sciences, Diss., 2002

[59] PUSCHNIG, P. ; MEISENBICHLER, C. ; DRAXL, C.: Excited State Properties of Organic Semiconductors: Breakdown of the Tamm-Dancoff Approximation. In: *ArXiv e-prints* (2013), jun

[60] QUARTI, Claudio ; MOSCONI, Edoardo ; DE ANGELIS, Filippo: Structural and electronic properties of organo-halide hybrid perovskites from ab initio molecular dynamics. In: *Phys. Chem. Chem. Phys.* 17 (2015), 9394-9409. http://dx.doi.org/10.1039/C5CP00599J. – DOI 10.1039/C5CP00599J

[61] REHR, J. J. ; ALBERS, R. C.: Theoretical approaches to x-ray absorption fine structure. In: *Rev. Mod. Phys.* 72 (2000), Jul, 621–654. http://dx.doi.org/10.1103/RevModPhys.72.621. – DOI 10.1103/RevModPhys.72.621

[62] REHR, J J. ; SOININEN, J A. ; SHIRLEY, E L.: Final-state rule vs the Bethe-Salpeter equation for deep-core x-ray absorption spectra. In: *Physica Scripta* 2005 (2005), Nr. T115, 207. http://stacks.iop.org/1402-4896/2005/i=T115/a=052

[63] REHR, J.J. ; ANKUDINOV, A.L.: Progress in the theory and interpretation of {XANES}. In: *Coordination Chemistry Reviews* 249 (2005), Nr. 1–2, 131 - 140. http://dx.doi.org/http://dx.doi.org/10.1016/j.ccr.2004.02.014. – DOI http://dx.doi.org/10.1016/j.ccr.2004.02.014. – ISSN 0010–8545. – Synchrotron Radiation in Inorganic and Bioinorganic Chemistry

[64] ROHLFING, Michael ; LOUIE, Steven G.: Electron-hole excitations and optical spectra from first principles. In: *Phys. Rev. B* 62 (2000), Aug, 4927–4944. http://dx.doi.org/10.1103/PhysRevB.62.4927. – DOI 10.1103/PhysRevB.62.4927

[65] SAGMEISTER, S.: *Excitonic Effects in Solids: Time-Dependent Density Functional Theory versus the Bethe-Salpeter Equation*, Karl-Franzens-Universität Graz, Faculty of Natural Sciences, Diss., 2009

[66] SANDER, Tobias ; MAGGIO, Emanuele ; KRESSE, Georg: Beyond the Tamm-Dancoff approximation for extended systems using exact diagonalization. In: *Phys. Rev. B* 92 (2015), Jul, 045209. http://dx.doi.org/10.1103/PhysRevB.92.045209. – DOI 10.1103/PhysRevB.92.045209

[67] SHAM, L. J. ; RICE, T. M.: Many-Particle Derivation of the Effective-Mass Equation for the Wannier Exciton. In: *Phys. Rev.* 144 (1966), Apr, 708–714. http://dx.doi.org/10.1103/PhysRev.144.708. – DOI 10.1103/PhysRev.144.708

[68] SHIRLEY, Eric L.: Bethe–Salpeter treatment of X-ray absorption including core-hole multiplet effects. In: *Journal of Electron Spectroscopy and Related Phenomena* 144–147 (2005), 1187 - 1190. http://dx.doi.org/http://dx.doi.org/10.1016/j.elspec.2005.01.191. – DOI http://dx.doi.org/10.1016/j.elspec.2005.01.191. – ISSN 0368–2048. – Proceeding of the Fourteenth International Conference on Vacuum Ultraviolet Radiation Physics

[69] SINGH, David: Ground-state properties of lanthanum: Treatment of extended-core states. In: *Phys. Rev. B* 43 (1991), Mar, 6388–6392. http://dx.doi.org/10.1103/PhysRevB.43.6388. – DOI 10.1103/PhysRevB.43.6388

[70] SINGH, David J.: *Planewaves, Pseudopotentials and the LAPW Method.* Boston/Dordrecht/London : Kluwer Academic Publishers, 1994. – ISBN 0–7923–9412–7

[71] SJÖSTEDT, E ; NORDSTRÖM, L ; SINGH, D.J: An alternative way of linearizing the augmented plane-wave method. In: *Solid State Communications* 114 (2000), Nr. 1, 15 - 20. `http://dx.doi.org/http://dx.doi.org/10.1016/S0038-1098(99)00577-3`. – DOI http://dx.doi.org/10.1016/S0038–1098(99)00577–3. – ISSN 0038–1098

[72] STOUMPOS, Constantinos C. ; MALLIAKAS, Christos D. ; KANATZIDIS, Mercouri G.: Semiconducting Tin and Lead Iodide Perovskites with Organic Cations: Phase Transitions, High Mobilities, and Near-Infrared Photoluminescent Properties. In: *Inorganic Chemistry* 52 (2013), Nr. 15, 9019-9038. `http://dx.doi.org/10.1021/ic401215x`. – DOI 10.1021/ic401215x. – PMID: 23834108

[73] TURKINA, Olga: *Optical excitations in rutile and anatase TiO_2 investigated by many-body perturbation theory*, Humbolt-Universität Berlin, Master Thesis, 2013

[74] UMARI PAOLO ; MOSCONI EDOARDO ; DE ANGELIS FILIPPO: Relativistic GW calculations on CH3NH3PbI3 and CH3NH3SnI3 Perovskites for Solar Cell Applications. In: *Scientific Reports* 4 (2014), mar, 4467. `http://dx.doi.org/http://dx.doi.org/10.1038/srep0446710.1038/srep04467`. – DOI http://dx.doi.org/10.1038/srep04467 10.1038/srep04467

[75] UMEBAYASHI, T. ; ASAI, K. ; KONDO, T. ; NAKAO, A.: Electronic structures of lead iodide based low-dimensional crystals. In: *Phys. Rev. B* 67 (2003), Apr, 155405. `http://dx.doi.org/10.1103/PhysRevB.67.155405`. – DOI 10.1103/PhysRevB.67.155405

[76] VINSON, J. ; REHR, J. J. ; KAS, J. J. ; SHIRLEY, E. L.: Bethe-Salpeter equation calculations of core excitation spectra. In: *Phys. Rev. B* 83 (2011), Mar, 115106. `http://dx.doi.org/10.1103/PhysRevB.83.115106`. – DOI 10.1103/PhysRevB.83.115106

[77] WADDINGTON, W. G. ; REZ, P. ; GRANT, I. P. ; HUMPHREYS, C. J.: White lines in the L_2, *3* electron-energy-loss and x-ray absorption spectra of *3d* transition metals. In: *Phys. Rev. B* 34 (1986), Aug, 1467–1473. `http://dx.doi.org/10.1103/PhysRevB.34.1467`. – DOI 10.1103/PhysRevB.34.1467

[78] WESTENBRINK, H. G. ; TERPSTRA, P.: On the crystal structure of lead-iodide. In: *Proceedings of the Koninklijke Nederlandse Academie van Wetenschappen* 29 (1926), Nr. 3, S. 431–442

[79] YANG, Woon S. ; NOH, Jun H. ; JEON, Nam J. ; KIM, Young C. ; RYU, Seungchan ; SEO, Jangwon ; SEOK, Sang I.: High-performance photovoltaic perovskite layers fabricated through intramolecular exchange. In: *Science* 348 (2015), Nr. 6240, 1234–1237. `http://dx.doi.org/10.1126/science.aaa9272`. – DOI 10.1126/science.aaa9272. – ISSN 0036–8075

[80] YIN, Wan-Jian ; SHI, Tingting ; YAN, Yanfa: Unusual defect physics in CH3NH3PbI3 perovskite solar cell absorber. In: *Applied Physics Letters* 104 (2014), Nr. 6. `http://dx.doi.org/http://dx.doi.org/10.1063/1.4864778`. – DOI http://dx.doi.org/10.1063/1.4864778

[81] YNDURÁIN, Francisco J.: Spin 1/2 Particles. Version: 1996. `http://dx.doi.org/10.1007/978-3-642-61057-8_3`. In: *Relativistic Quantum Mechan-*

ics and Introduction to Field Theory. Springer Berlin Heidelberg, 1996 (Texts and Monographs in Physics), 35-66

[82] ZAANEN, J. ; SAWATZKY, G. A. ; FINK, J. ; SPEIER, W. ; FUGGLE, J. C.: L_2, 3 absorption spectra of the lighter *3d* transition metals. In: *Phys. Rev. B* 32 (1985), Oct, 4905–4913. `http://dx.doi.org/10.1103/PhysRevB.32.4905.–` DOI 10.1103/PhysRevB.32.4905

Selbständigkeitserklärung

Hiermit versichere ich, dass ich die vorliegende Arbeit selbstständig verfasst habe und keine anderen als die angegebenen Quellen und Hilfsmittel verwendet habe.

Berlin, den

Unterschrift